Diffusion and ionic conduction in nanocrystalline ceramics

2003 J. Phys.: Condens. Matter 15 R1257

(http://iopscience.iop.org/0953-8984/15/30/202)

INSTITUTE OF PHYSICS PUBLISHING JOURNAL OF PHYSICS: CONDENSED MATTER

J. Phys.: Condens. Matter **15** (2003) R1257–R1289 PII: S0953-8984(03)23478-0

TOPICAL REVIEW

Diffusion and ionic conduction in nanocrystalline ceramics

Paul Heitjans and Sylvio Indris

Institut für Physikalische Chemie und Elektrochemie, Universität Hannover, Callinstraße 3-3A, 30167 Hannover, Germany

E-mail: heitjans@pci.uni-hannover.de and indris@pci.uni-hannover.de

Received 19 May 2003, in final form 9 June 2003
Published 18 July 2003
Online at stacks.iop.org/JPhysCM/15/R1257

Abstract

We review case studies of diffusion in nanocrystalline ceramics, i.e. polycrystalline non-metallic materials with average grain sizes typically in the range from 5 to 50 nm. The experimental methods applied are, on the one hand, tracer diffusion or conductivity methods which are sensitive to macroscopic transport, and, on the other hand, NMR techniques which, complementarily to the previous ones, give access to microscopic diffusion parameters like atomic hopping rates and jump barrier heights. In all cases the diffusion properties of the samples, whether single-phase systems or composites, are dominated by their grain boundaries and interfacial regions, respectively. In principle, all experimental techniques allow one to discriminate between contributions to the diffusion from the crystalline grains and those from the interfacial regions. Corresponding examples are presented for SIMS and impedance measurements on oxygen conductors. NMR studies for various nanocrystalline lithium ion conductors reveal that two lithium species with different diffusivities are present. Comparison with the coarse grained counterparts shows that the slower ions are located inside the crystallites and the faster ones in the structurally disordered interfacial regions. Investigations on composite materials exhibit phenomena which can be explained by the percolation of fast diffusion pathways being formed by the interfaces between the two components.

Contents

1. Introduction

The advent of nanostructured materials in recent years has inspired many new developments in solid state physics, solid state chemistry and materials science. Due to a tailored microstructure these materials can show new mechanical [1–4], electrical [5–9], magnetic [10–15], optical [16–20], catalytic [21, 22] and thermodynamic [23–25] properties. This is due to the increased fraction of structurally disordered interfacial regions, enhanced surface area or quantum confinement effects. Besides the investigation of the structural features of nanostructured solids *per se*, the challenge is to study those macroscopic properties and to interrelate them to the microscopic structure. Diffusion processes in these solids are often important for this interrelation. They are influenced by the microstructure and, in turn, determine a number of macroscopic properties.

Whereas earlier reviews concentrate on diffusion studies in single crystalline or coarse grained ceramics on the one hand [26] and nanocrystalline *metals* on the other hand [27, 28], this review reports on experimental investigations of diffusion in nanocrystalline ceramics. The first theoretical approaches concerning diffusion in nanocrystalline materials so far deal with metallic systems [29–31].

Ceramics are traditionally defined as the products of firing nonmetallic minerals at high temperatures [32]. Some categories are silicate ceramics, nonsilicate oxide ceramics, non-oxide ceramics, glass ceramics and ceramic composite systems. They are characterized by high chemical and thermal stability but poor mechanical properties, brittleness in particular. In this review we refer to the more general definition of ceramics as non-metallic, inorganic materials [33, 34]. The macroscopic behaviour of ceramics, such as plastic deformation, sintering or reactivity, is often governed by atomic diffusion in these solids [35, 36]. Furthermore, diffusion in ceramics by itself is important since diffusion in ionic crystals is related to ion transport and thus to electrical conductivity. This leads to solid electrolytes, which may find applications in battery systems, fuel cells or sensors.

In nanocrystalline semiconductors, additionally to the increased volume fraction of interfacial regions influencing ionic conduction, quantum effects can also play an important role. Due to quantum confinement of the electronic charge carriers in the small grains an increase of the band gap can occur. This results in a blue shift of the absorption edge in, for example, nanocrystalline TiO_2 [21], CdS_2 [16] and $CdSe_2$ [17] for crystallites smaller than about 10 nm.

Because of the numerous possible applications many efforts are being made to synthesize nanocrystalline materials. However, such materials also play a role in some phenomena of daily life, for example the colouration of glass windows in old churches was achieved by inclusion of nanocrystalline metal particles in the glass matrix and the occurrence of ball lightning is ascribed to inhibited oxidation of nanocrystalline Si/SiO particles [37].

Up to now many studies have been made concerning electronic conductivity in nanocrystalline semiconductors, e.g. [7–9]. Ionic conductivity and diffusion in nanocrystalline ceramics has been studied less intensively, in contrast to the impact for, for example, catalytic or sensor properties of these solids. For ionic systems the formation of ionic space charge layers is expected to increase the ionic conductivity parallel to the interfaces [38, 39]. This effect will be more pronounced in nanocrystalline materials [40, 41]. The preparation of nanocrystalline materials itself can also be diffusion-controlled, e.g. when they are prepared by transformation of an amorphous phase [42].

This review is organized as follows. In section 2 we give a classification of the different types of nanostructured materials of which nanocrystalline solids represent a subgroup. The preparation and characterization of nanocrystalline ceramics dealt with here are summarized in section 3. Section 4 briefly recalls some fundamentals of diffusion and ionic conduction. An overview of the experimental techniques applied so far to nanocrystalline ceramics is given in section 5. Illustrative experimental results, obtained both on single-phase and composite materials, are presented in section 6. Conclusions are drawn in section 7.

2. Classification of nanostructured materials

Nanostructured or nanoscaled solids are materials with structural length scales shorter than 100 nm in at least one dimension [23, 43–47]. Figure 1 gives an overview, presenting a classification of nanostructured materials.

A special category is assigned to nano*crystalline* materials (upper row of figure 1). These are polycrystalline materials with an average grain size typically in the range from 5 to 50 nm. The crystalline grains are represented in figure 1 by regular lattices with an atom at each lattice site. Between the randomly oriented crystallites there are grain boundaries or interfacial regions. Reducing the crystallite size to some nanometres and assuming that the average interface thickness ranges from 0.5 to 1 nm, the volume fraction of interfacial regions can be as high as 50% [44, 48]. So nanocrystalline materials are solids consisting of crystallites with length scales in the nanometre regime in all three dimensions.

When these short length scales show up only in one or two dimensions the material consists of crystalline layers and rods, respectively. This is depicted in the lower row of figure 1. Diffusion in such materials will be anisotropic and one is able to discern diffusion *along* and *across* the interfacial regions by macroscopic diffusion measurements. The middle column of figure 1 shows a generalization where the crystalline regions are built of two different crystallites yielding composite materials. Furthermore the nanocrystals can be isolated and embedded in a matrix material being crystalline or amorphous (right column of figure 1).

A key point is whether the grain boundaries or interfacial regions in nanocrystalline materials are crystallographically well defined by the regular structure of the adjacent crystallites or are more glass-like[1], i.e. amorphous. The situation is indicated in a simplified way in figure 2 which shows hard sphere representations of single crystalline, nanocrystalline and amorphous solids. As is well known, single crystals are characterized by long-range

[1] The early notion of an even *gas-like* structure of the inferfaces is apparently no longer favoured in the literature [49, 50].

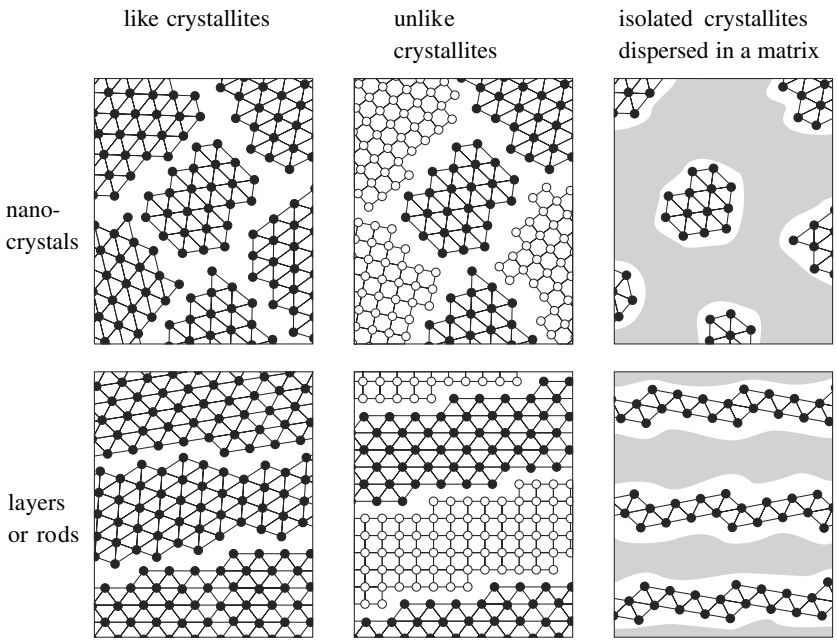

Figure 1. Classification of nanostructured materials. The top row shows nanocrystalline materials with length scales in the nanometre regime in all three dimensions. The bottom row presents low-dimensional systems where the nanocrystalline regions are restricted to one or two dimensions, resulting in layered and rod-shaped structures, respectively. The middle column shows composite materials consisting of two different types of grains and the right column is a generalization with isolated nanocrystals embedded in a host matrix. This matrix can be crystalline or amorphous.

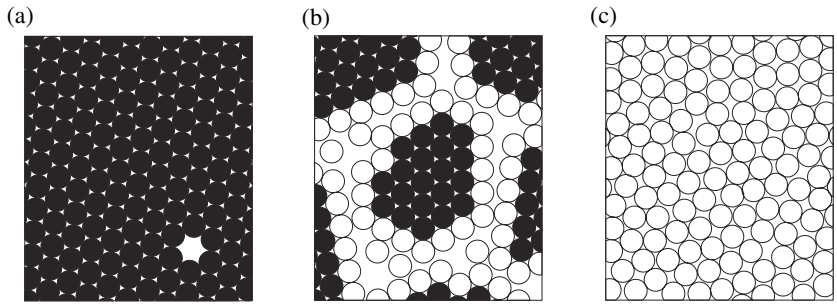

Figure 2. Sketches of (a) crystalline (with vacancy), (b) nanocrystalline, (c) amorphous solids.

translational symmetry and transport can only occur via point defects like vacancies or interstitials (figure 2(a)). The concentration of intrinsic defects in thermal equilibrium increases with temperature, which means for ionic crystals that the concentration of charge carriers is temperature-dependent [26, 36]. This is not true for extrinsic defects which are generated by aliovalent impurities. Amorphous solids (figure 2(c)) do not show long-range but short-range order, saying that interatomic distances and coordination numbers are still similar for all atoms. Accordingly, one may conceive of nanocrystalline solids ('*cum nano-grano salis*') as consisting of atoms in structurally ordered crystallites and atoms located in structurally disordered interfaces. Thus, in contrast to amorphous materials showing *homogeneous*

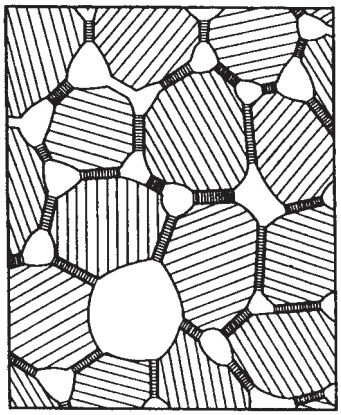

Figure 3. Sketch of a nanocrystalline material with crystalline grains, interfacial regions and a large volume fraction of pores [64].

disorder, nanocrystalline materials may be regarded as *heterogeneously* disordered with ordered grains and disordered interfaces. The degree of disorder may vary from the glass-like structure considered above to a structure where the interface atoms occupy regular lattice sites but have reduced coordination numbers and which may be classified as highly defective (figure 2(b)). Thus the structure of nanocrystalline materials appears to be somewhere intermediate between those of crystalline and amorphous solids.

Concerning metallic nanocrystalline materials, on the one hand molecular dynamics studies show that the interfacial regions exhibit a higher degree of disorder than grain boundaries in bicrystals [51–53]. On the other hand, some experimental results contradict this view, e.g. extended x-ray absorption fine structure (EXAFS) analysis of nanocrystalline copper indicates that the local structure in the grain boundaries of this metal is similar to that in the coarse grained counterpart, i.e. the atoms are *not* randomly distributed [54]. More recent molecular dynamics investigations seem to support these results [55]. As for nanocrystalline *ceramics*, the microstructure is even less well studied and a matter of debate, too. In any case, the degree of disorder encountered in the interfacial regions will depend on the specific substance and the preparation technique applied to produce the nanocrystalline material.

In grain boundaries many atoms have a reduced coordination number with respect to the grain interior and the local density is smaller, which leads to an enhanced diffusivity of the atoms. This is well known for the grain boundaries in coarse grained metals [56, 57]. Since in nanocrystalline metals the number of grain boundaries is strongly increased the enhancement of diffusivity can be more pronounced [28, 58] and such an effect is expected to be found also in ceramic systems. In addition to the grain boundaries, a further structural element which occurs with high concentration in nanocrystalline materials are triple junctions, i.e. the borderlines where three adjacent crystallites are brought into contact. These may form channels with vacancy-like sites and thus fast diffusion pathways, as predicted by theory [31]. First experimental confirmation is found for triple junctions in coarse grained copper [59]. For nanocrystalline iron–nickel alloys, however, the influence of triple junction diffusion turned out to be negligible [60]. In nanocrystalline ceramic materials one has to take into account that the volume fraction of pores can be as high as 20% [61–63], as illustrated in figure 3 [64]. For diffusion studies this implies that, besides contributions from the bulk and the interfaces, surface diffusion can also occur.

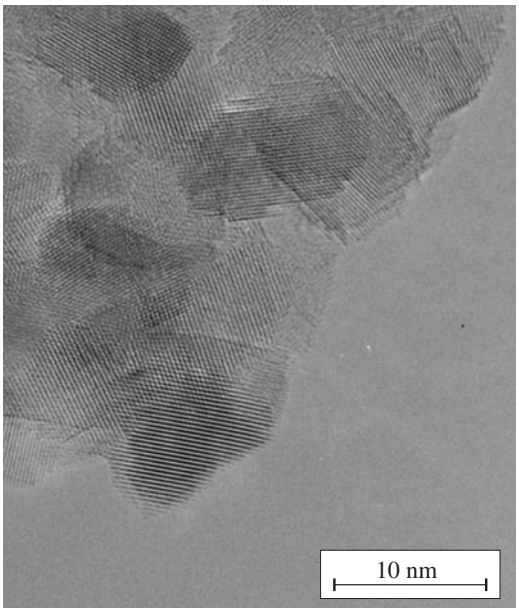

Figure 4. High resolution TEM micrograph of nanocrystalline CaF_2 prepared by IGC (cf [80]).

3. Preparation and characterization of nanocrystalline ceramics

There are many methods by which nanocrystalline materials may be prepared. In principle, there are two approaches to building a nanocrystal. One way is to assemble it from separate atoms (or molecules), e.g. from the gas phase or from solution. Examples are inert gas condensation (IGC) [23, 65], chemical vapour synthesis (CVS) [66], sol–gel methods [67], pulsed electrodeposition [68] and reverse microemulsion techniques [69, 70]. Using CVS with various experimental set-ups Srdic *et al* [66] were able to produce, besides pure ZrO_2, ZrO_2 doped with Al_2O_3, mixtures of ZrO_2 and Al_2O_3 and also ZrO_2 coated with Al_2O_3.

The alternative approach to get to a nanocrystalline material is to start with a coarse grained material and to reduce the grain size by mechanical attrition, e.g. by ball milling [71–73]. The advantages of ball milling are the fact that almost every material is accessible, that large amounts can be produced and that the average grain size can easily be varied by choice of the milling time. This method is therefore useful when many different materials are to be compared. One disadvantage of ball milling is that abrasion of the milling vial may occur. This has to be minimized by choosing appropriate materials for the milling vial and balls, respectively, and a definite ball-to-powder weight ratio. To produce compacted solids from the loose powders a sintering process is required and one has to accept partial grain growth [48, 74]. Chen *et al* [75] have shown that two-step sintering with reduced temperature in the second step can give fully dense ceramics with reduced grain growth.

Concerning the characterization of nanocrystalline materials, the main objectives are the determination of the average grain size and the distribution of grain sizes. Most direct information is obtained by using transmission electron microscopy (TEM) [76–78]. Figure 4 shows an example of nanocrystalline CaF_2 with an average grain size of about 9 nm which was prepared by IGC [79, 80]. The high resolution of this micrograph makes it possible to identify various crystallites with different crystallographic orientations.

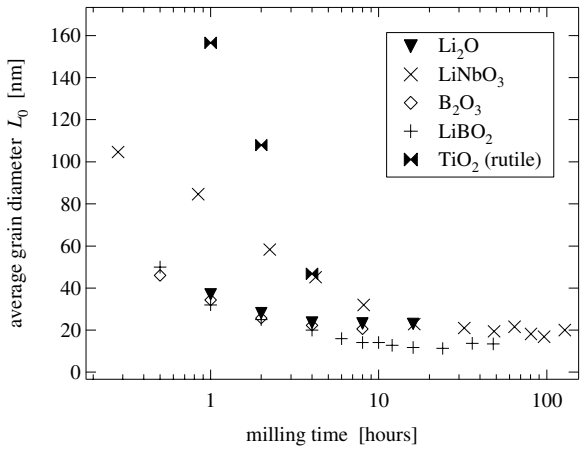

Figure 5. Average grain size versus milling time for some oxide ceramics prepared by high-energy ball milling, after [73, 87, 88].

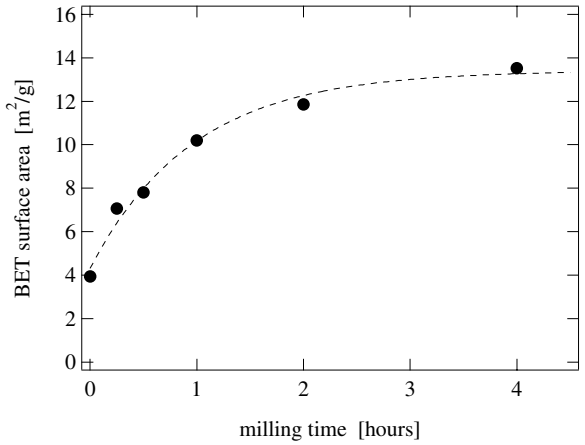

Figure 6. BET surface area of nanocrystalline TiO_2 (rutile) powders increasing with milling time, after [88].

Since sample preparation may be elaborate for TEM and microscopes with atomic resolution are rare, the most common method for the determination of grain sizes is x-ray diffraction (XRD) [81, 82]. From the broadening of the XRD lineshapes the average crystallite size L_0 can be determined. The simplest approach is to use the Scherrer formula

$$L_0 = \frac{K\lambda}{\beta \cos\theta}, \tag{1}$$

where K is a constant of the order of unity, being dependent on the crystallite shape (0.89 for spherical particles), λ is the wavelength of x-ray radiation, θ is the diffraction angle and β is the width of the XRD line after corrections for instrumental broadening. A more sophisticated analysis of the exact lineshapes can also give the distribution of crystallite sizes [83, 84]. In addition, information on internal stress can be obtained from the XRD measurements [85]. Figure 5 shows results from XRD analysis of some oxide ceramics which were prepared by ball milling of the coarse grained source materials [73, 86–88]. A high-energy ball mill

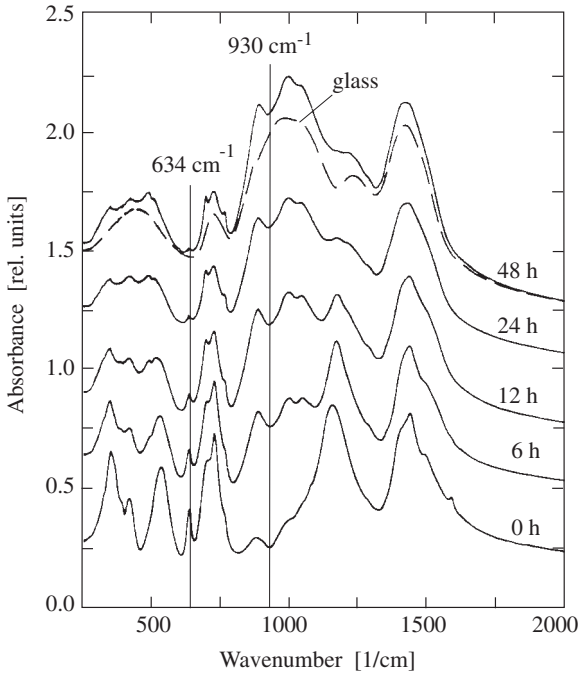

Figure 7. Infrared spectra of nanocrystalline $LiBO_2$ ballmilled for various times compared to the unmilled sample and the glassy material (broken curve), after [90].

(SPEX 8000) with an alumina vial and a single ball was used. The ball-to-powder weight ratio was typically 2:1. One can notice two time regimes for all the samples. For short times up to about 5 h the average grain size L_0 decreases with increasing milling time. For longer milling times a saturation behaviour with a final grain size of about 20 nm shows up. Such a saturation behaviour was found earlier also for metals and alloys [89].

Further standard methods to investigate nanocrystalline materials include BET surface area characterization, which gives information about secondary particle sizes (agglomeration of crystallites), and differential scanning calorimetry (DSC) to study the thermal stability of the samples. As an example figure 6 shows the BET surface area of nanocrystalline TiO_2 (rutile) as a function of milling time. Again a saturation behaviour is observed which qualitatively corresponds to that of the average grain size of n-TiO_2 (cf figure 5).

Figure 7 shows infrared (IR) spectra of ballmilled $LiBO_2$ compared to the unmilled sample and the glassy material [90]. The unmilled source material is a mixture of the two crystalline phases α-$LiBO_2$ and γ-$LiBO_2$. α-$LiBO_2$ consists of $[BO_3]$ triangles which are interconnected by the Li ions and shows characteristic peaks at 634 and 1150 cm^{-1}. γ-$LiBO_2$ is composed of $[BO_4]$ tetrahedra whose stretching modes give a characteristic peak at 775 cm^{-1}, which decreases with increasing milling time. In the course of milling the peaks of the crystalline phases are decreasing and a broad peak arises at about 930 cm^{-1}, which is characteristic of the spectrum of the glassy material shown as a broken curve. One notices that with increasing milling time the overall spectra of the nanocrystalline materials become very similar to the spectrum of the glassy material, which suggests that the interfaces created by ball milling are amorphous, at least for this material.

More sophisticated techniques for the characterization of nanocrystalline materials are electron diffraction [91], positron annihilation spectroscopy [92] and EXAFS

measurements [93, 94]. These methods can be used to probe the different environments of atoms being located in the crystalline grains and in the interfacial regions, respectively.

4. Fundamentals of diffusion and ionic conduction

Diffusion is the process of particle movement driven by a concentration gradient [95]. Fick's first law relates the particle flux $\boldsymbol{j}_p$ to the gradient of concentration c of these particles:

$$\boldsymbol{j}_p = -D^{\mathrm{T}} \nabla c. \tag{2}$$

D^{T} is called the tracer diffusion coefficient or diffusivity. Combining equation (2) with the continuity equation:

$$\frac{\partial c}{\partial t} + \nabla \boldsymbol{j}_p = 0, \tag{3}$$

results in Fick's second law:

$$\frac{\partial c}{\partial t} = \nabla (D^{\mathrm{T}} \nabla c). \tag{4}$$

This partial differential equation simplifies if D^{T} is constant and can be solved for particular initial and boundary conditions [96]. This allows one to determine D^{T} from measurements of concentration profiles $c(\boldsymbol{r}, t)$. The temperature dependence of the diffusion coefficient is often described empirically by an Arrhenius relation

$$D^{\mathrm{T}} = D_0^{\mathrm{T}} \exp\left(-\frac{E_{\mathrm{A}}}{k_{\mathrm{B}} T}\right) \tag{5}$$

where E_{A} is the activation energy for the mass transport, D_0^{T} is the pre-exponential factor, k_{B} is the Boltzmann constant and T is the temperature.

From the microscopic point of view, the tracer diffusion coefficient D^{T} can be defined by the Einstein–Smoluchowski relation [97, 98]

$$D^{\mathrm{T}} = \lim_{t \to \infty} \frac{\langle r^2(t) \rangle}{2dt}. \tag{6a}$$

Here $\langle r^2(t) \rangle$ is the mean square displacement of the particles after the time t and d is the dimensionality of the movement.

An atom moving through a solid will perform jumps between different minima in a potential landscape. In crystalline solids these minima are represented by lattice sites or interstitial sites. In general, the potential landscape may be time dependent [99]. Considering the case where the mean jump time is short compared to the mean residence time τ in such a minimum, the trajectory of a particle is composed of a sequence of elementary jumps with average jump length ℓ. From these microscopic quantities a diffusion coefficient D^{uc} for uncorrelated jumps can be defined by

$$D^{\mathrm{uc}} = \frac{\ell^2}{2d\tau}. \tag{6b}$$

The diffusion coefficients D^{T} and D^{uc} are related by

$$D^{\mathrm{T}} = f D^{\mathrm{uc}} \tag{7}$$

where f is the correlation factor. f equals unity if the movement is purely random hopping. For correlated motion of the atoms with enhanced backward hopping probability after completed jumps one has $0 < f < 1$.

In structurally ordered, i.e. single crystalline, systems defects are required for the movement of atoms or ions [36, 100]. Starting from a single crystalline material, introducing

such defects and thus disorder leads to increasingly defective systems, i.e. so-called highly defective single crystals, micro-/nanocrystalline materials and amorphous systems. The defects can be zero-dimensional (e.g. vacancies or interstitials), one-dimensional (dislocations) or two-dimensional (grain boundaries) defects. The highest degree of disorder can be found in amorphous materials. One point of interest is to investigate whether there is a correlation between structural disorder and the appearance of fast diffusion of atoms or ions. Such a correlation was shown to exist by, for example, comparative NMR relaxation studies of Li diffusion in glassy and crystalline $LiAlSiO_4$ [101], $LiAlSi_2O_6$ [101, 102] and $LiAlSi_4O_{10}$ [103]. Furthermore, a comparison between two different crystalline modifications of Li_xTiS_2, namely the hexagonal and the cubic structure [104], showed the influence of the dimensionality of the diffusion pathways on diffusivity.

A rather direct access to the diffusion of charged particles can be obtained by impedance spectroscopy, i.e. measurements of ac conductivities. From these the dc conductivity, i.e. the limit for very low frequencies, can be extracted and, by comparison with simple equivalent circuits, contributions of different structural elements of the samples may be discriminated (see section 5.3). The Nernst–Einstein equation

$$D^{\sigma} = \frac{\sigma_{\mathrm{dc}} k_{\mathrm{B}} T}{N q^2} \tag{8}$$

gives a direct relationship between ionic dc conductivity σ_{dc} and the diffusion coefficient D^{σ}. Here N is the particle density of the charge carriers and q is their charge. In general the conductivity of a material consists of a superposition of the contributions of all charge carriers like anions, cations, electrons and holes. Discrimination between the various contributions may be achieved via selectively blocking electrodes. The diffusion coefficient D^{σ} obtained from conductivity measurements via equation (8) is related to the tracer diffusion coefficient D^{T} by

$$D^{\mathrm{T}} = H_{\mathrm{R}} D^{\sigma}. \tag{9}$$

Here H_{R} is the Haven ratio which gives information on whether conductivity is based on one charge carrier or a superposition of several contributions [105, 106]. In the special case of single ions and random jumps it holds that $H_{\mathrm{R}} = f = 1$, i.e. $D^{\mathrm{T}} = D^{\sigma} = D^{\mathrm{uc}}$. One gets $H_{\mathrm{R}} < 1$ when correlations occur in the movement of the charge carriers or when electronic conduction is present. When defects like vacancy pairs or impurity–vacancy pairs participate in the diffusion which are not 'seen' in conductivity one obtains $H_{\mathrm{R}} > 1$.

As is well known, in the linear response theory the fluctuation–dissipation theorem relates the microscopic fluctuations in a system in thermal equilibrium to its dissipation, i.e. the power absorbed, and thus to its macroscopic relaxation behaviour. A special formulation of the fluctuation–dissipation theorem is expressed in the Kubo formula [107, 108]

$$\sigma(\omega) = \frac{L^d}{k_{\mathrm{B}} T d} \int_0^{\infty} \langle \boldsymbol{j}(0) \boldsymbol{j}(t) \rangle \, \mathrm{e}^{\mathrm{i}\omega t} \, \mathrm{d}t, \tag{10}$$

which relates the frequency-dependent conductivity to the autocorrelation function of the current density $\boldsymbol{j}$. L^d is in the three-dimensional case the volume of the sample. In the absence of interaction between the mobile ions, equation (10) can be used to derive a generalized form of the Nernst–Einstein equation (equation (8)) [108]:

$$\sigma(\omega) = \frac{N q^2}{k_{\mathrm{B}} T} D^{\sigma}(\omega) \tag{11}$$

with a frequency-dependent diffusion coefficient

$$D^{\sigma}(\omega) = -\frac{\omega^2}{2d} \int_0^{\infty} \langle r^2(t) \rangle \, \mathrm{e}^{\mathrm{i}\omega t} \, \mathrm{d}t. \tag{12}$$

Table 1. Some macroscopic/microscopic and nuclear/non-nuclear methods for studying diffusion in solids, after [109].

	Macroscopic	Microscopic
Nuclear		
	Tracer diffusion	NMR relaxation
		β-radiation-detected NMR
	Field gradient NMR	Quasielastic neutron scattering
		Mössbauer spectroscopy
Non-nuclear		
	DC conductivity	AC conductivity
	Mechanical relaxation	

This relates the time-dependent mean square displacement of the charge carriers to the ac conductivity.

5. Outline of diffusion measurement techniques

5.1. Survey

There are numerous experimental methods for studying diffusion in solids. Table 1 gives an overview [109]. The methods can be subdivided into macroscopic methods, which are sensitive to long-range diffusion, and into microscopic methods, which give access to microscopic diffusion parameters like hopping rates of atoms or ions and the barrier heights for the jump processes. Examples of macroscopic methods are tracer diffusion techniques, where concentration profiles in solids are evaluated, NMR measurements in a magnetic field gradient (FG-NMR), dc conductivity measurements and mechanical relaxation spectroscopy. Microscopic methods are, for example, NMR relaxation spectroscopy (incorporating spin–lattice relaxation and spin–spin relaxation, i.e. lineshape measurements), β-radiation-detected NMR (β-NMR), quasielastic neutron scattering (QENS), Mössbauer spectroscopy (MS) and ac conductivity [110]. As implemented in table 1, a further way to classify these diffusion measurement techniques is to distinguish between nuclear and non-nuclear methods. Nuclear methods are those which use radioactive or stable nuclei or elementary particles as probes.

Figure 8 shows typical ranges of the diffusivity D^{T} (upper abscissa) and motional correlation time τ_{c} (lower abscissa) for macroscopic and microscopic methods, respectively. τ_{c} (see section 5.5) has been converted to D^{T} via equation (6) adopting a typical jump length in solids of some ångströms. Three-dimensional, uncorrelated diffusion with a mean residence time equal to the correlation time was assumed. The length scale for the diffusion processes which are probed by methods like impedance spectroscopy (measuring ac conductivities, see section 5.3) or NMR relaxation spectroscopy (sections 5.4 and 5.5) varies with the applied measurement frequency and so a combination of different techniques and/or experimental set-ups may be desirable.

Combining the results of macroscopic and microscopic methods one is able to evaluate the correlation factor f. This finally gives information about the observed diffusion mechanism [111]. For example, the (direct) interstitial mechanism is characterized by $f = 1$ and the vacancy mechanism in a bcc lattice by $f = 0.727$ [112, 113]. Furthermore it depends on the specific frequency range of each method whether preferably long-range or short-range diffusion is probed.

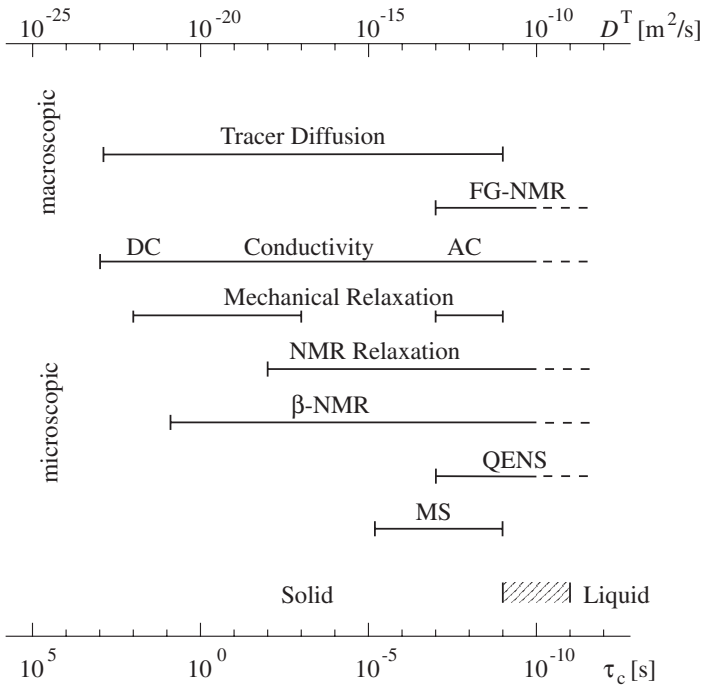

Figure 8. Typical ranges of the diffusivity D^{T} and motional correlation time τ_{c} of some macroscopic and microscopic methods, respectively, for studying diffusion in solids, after [109]. FG-NMR: field gradient NMR, β-NMR: β-radiation-detected NMR, QENS: quasi-elastic neutron scattering, MS: Mössbauer spectroscopy. The hatched bar indicates the transition from the solid to the liquid where the motional correlation time is reduced by about two orders of magnitude.

Up to now diffusion in nanocrystalline ceramics has been studied by tracer diffusion methods, conductivity measurements, NMR lineshape studies and NMR spin–lattice relaxation techniques, and we will confine ourselves to these methods, which will be introduced briefly in sections 5.2–5.5. When applicable, additional methods like QENS [114], β-NMR [101], muon spin resonance/relaxation (μSR) spectroscopy [115, 116] or deuterium effusion experiments [117] can give a deeper insight into the diffusion mechanisms.

5.2. Tracer diffusion method

An example of a method which is sensitive to macroscopic diffusion is the tracer method [95]. A tracer may be a radioactive or a stable isotope which can be tracked by its radioactive emission or its mass. This tracer isotope is deposited on the surface of the specimen. The specimen is then diffusion-annealed in a furnace at the temperature T at which the diffusion coefficient is to be measured. In the case of radioactive tracers the time for annealing has to be short compared to the lifetime of the radioisotope. Then the concentration profiles of the tracer are determined. For penetration depths larger than 1 μm classical radiotracer techniques can be used, which implies mechanical sectioning of the specimen and subsequent measurement of radioactivity of the layers. By contrast, SIMS (secondary ion mass spectrometry) profiling is applicable for penetration depths smaller than 1 μm. The surface of the specimen is bombarded with a beam of primary ions, which results in a continuous atomization of the sample. The sputtered secondary ions can then be detected in a mass spectrometer.

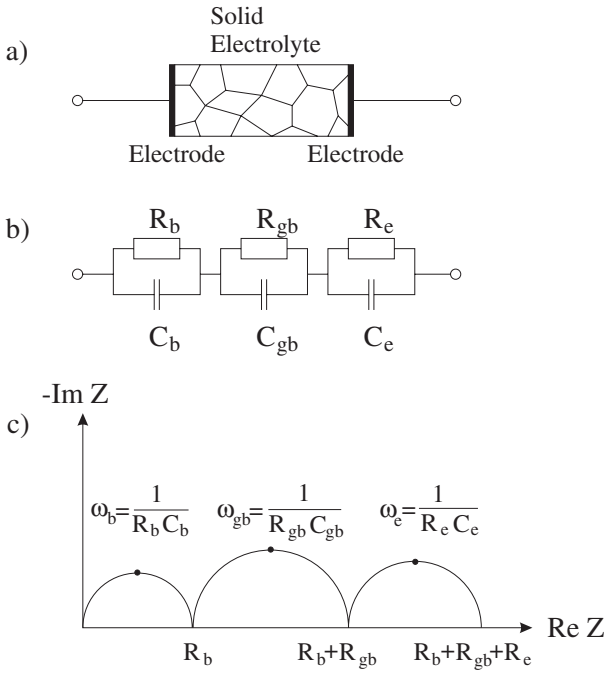

Figure 9. (a) Polycrystalline solid electrolyte with contacts, (b) equivalent circuit with contributions from (the bulk of) the grains, the grain boundaries and the electrodes and (c) impedance plot for the case $\omega_b \gg \omega_{gb} \gg \omega_e$.

5.3. Impedance spectroscopy

Impedance spectroscopy, i.e. the measurement of complex resistivities with ac current methods, is an important tool to study diffusion in solids [118, 119]. A challenge concerning polycrystalline materials is to differentiate between contributions from different structural parts of the sample like bulk material or grain boundaries, i.e. to investigate the influence of the microstructure on the overall conductivity [120, 121].

Applying an ac voltage

$$U(\omega) = U_0 \, \mathrm{e}^{\mathrm{i}\omega t} \tag{13}$$

to a sample results in an ac current

$$I(\omega) = I_0 \, \mathrm{e}^{\mathrm{i}(\omega t + \Phi)} \tag{14}$$

having the same frequency as the voltage but, in general, a phase shift by an angle Φ. The complex impedance, consisting of a real and an imaginary part which belong to the conductive and capacitive components, respectively, of the current response to the applied voltage, is defined by Ohm's law:

$$Z(\omega) = \frac{U(\omega)}{I(\omega)} = Z_0 \, \mathrm{e}^{-\mathrm{i}\Phi} = Z_0 \cos\Phi - \mathrm{i} Z_0 \sin\Phi. \tag{15}$$

In many cases the impedance of a material can be described by simple equivalent circuits consisting of resistors, capacitors or inductances. Comparison with a conjectured microstructure can give information about its structural parameters [122–129]. This is sketched in figure 9. The bulk, the grain boundaries in the electrolyte and the interfaces to the electrodes

are each described by a simple *RC* circuit. These are connected in series. Calculating the overall impedance of this equivalent circuit and plotting the imaginary part versus the real part results in a diagram sketched in figure 9(c). Each *RC* component corresponds to a characteristic semicircle where the frequency as implicit parameter increases from right to left. The intercepts with the real axis give the resistivities and the apex frequencies yield the capacities of the different components of the equivalent circuit. Of course, this is a very idealized approach and in real systems the different semicircles can only be discriminated when the characteristic frequencies differ by more than, for example, three decades.

5.4. NMR lineshape spectroscopy

In general, nuclear spins I in an external magnetic field B_0 experiencing dipolar interaction in a homogeneous solid at low temperatures show one broad static NMR line without substructure. This is because the nuclei under investigation are located at sites with different spin environments, resulting in different local magnetic fields superimposed on the external magnetic field B_0. In this way many contributions with different resonance frequencies form a broad NMR line with a width of some kilohertz. This is the rigid lattice linewidth $\Delta\nu_R$ which corresponds to the spin–spin relaxation rate T_2^{-1} at low temperatures. When the sample is heated the ions start moving through the solid. The temperature dependence of the average jump rate is given by an Arrhenius relation

$$\tau^{-1} = \tau_0^{-1} \exp\left(-\frac{E_A}{k_B T}\right). \tag{16}$$

Here τ_0^{-1} is the pre-exponential factor and E_A is the activation energy. It should be noted that this activation energy E_A is not necessarily identical with that encountered in tracer diffusion (cf equation (5)) or dc conductivity measurements. These macroscopic methods usually yield larger activation energies than the microscopic ones (cf table 2) due to the different time windows they are sensing (cf figure 8).

At higher temperatures the hopping of the ions becomes so fast that they are experiencing the same average local field. This sets in when the jump rate becomes larger than the width of the rigid lattice line, i.e.

$$\tau^{-1} \gtrsim 2\pi\,\Delta\nu_R. \tag{17}$$

Then all nuclei have the same resonance frequency and a narrowed NMR line is observed. This phenomenon is called *motional narrowing*. The functional dependence of the linewidth on temperature allows one to determine τ_0 and E_A [130].

The situation when at even higher temperatures the hopping rate exceeds the Larmor frequency:

$$\tau^{-1} \gtrsim \omega_L, \tag{18}$$

is called *extreme motional narrowing*. Then the spin–spin relaxation rate T_2^{-1} and the spin–lattice relaxation rate T_1^{-1} should have the same value and the final NMR linewidth is determined by the inhomogeneity of the magnetic field. Additional contributions to the lineshape can occur for nuclei with a spin $I \geqslant 1$. These have a quadrupolar moment which interacts with electric field gradients, when present, due to low crystal symmetry at the site of the nuclei.

5.5. NMR spin–lattice relaxation spectroscopy

Besides NMR lineshape being related to spin–spin relaxation rate measurements, diffusion of atoms or ions in solids can also be studied by measurements of the spin–lattice relaxation rate T_1^{-1} of the corresponding nuclei [101, 131–134].

Table 2. Overview of results from diffusion studies on nanocrystalline ceramics. Results are given for the activation energy E_A, the diffusion coefficient D and the conductivity σ_{dc}. The temperature T refers to the given value of the diffusion coefficient or conductivity.

Material	Method	E_A (eV)	D ($m^2\ s^{-1}$)	σ_{dc} ($S\ m^{-1}$)	T (K)	Remarks	Reference
$LiNbO_3$	^{7}Li NMR	0.23					[136]
Li_xTiS_2	^{7}Li NMR	0.16					[137]
$LiBO_2$	Impedance	0.72		4×10^{-4}	400		[138]
$LiBO_2$	^{7}Li NMR	0.21					[138]
Li_2O	Impedance	0.95		5×10^{-6}	433		[139]
Li_2O	^{7}Li NMR	0.31					[140]
Li_2O:B_2O_3	Impedance	0.98		4×10^{-5}	433		[139]
Li_2O:B_2O_3	^{7}Li NMR	0.34					[140]
Li_2O:Al_2O_3	^{7}Li NMR	0.32					[141]
$ZrO_2(Y_2O_3)$	Impedance	0.83		2.4×10^{-4}	500	Bulk conduct.	[142]
$ZrO_2(Y_2O_3)$	Impedance	1.03		6.4×10^{-6}	500	Interface cond.	[142]
ZnO	Impedance	0.57		2.4×10^{-1}	833		[143]
CeO_2	Impedance	0.99		2.4×10^{-4}	625	[a]	[144]
CeO_2	Impedance	1.16		7.7×10^{-5}	625	[b]	[144]
$(CeO_2)_{0.5}(BiO_{1.5})_{0.5}$	Impedance	1.34		3.8×10^{-2}	673	Bulk conduct.	[145]
$(CeO_2)_{0.5}(BiO_{1.5})_{0.5}$	Impedance	1.17		3.8×10^{-2}	673	Interface cond.	[145]
$SrCe_{0.95}Yb_{0.05}O_3$	Impedance	0.96		5×10^{-2}	625	Thin-film sample	[146]
ZrO_2	^{18}O SIMS	2.29	7×10^{-19}		1000	Bulk diffusion	[147]
ZrO_2	^{18}O SIMS	1.95	5×10^{-15}		1000	Interface diff.	[147]
TiO_2	^{18}O SIMS	0.43	4×10^{-16}		920		[64]
TiO_2	Impedance	1.00		3×10^{-4}	850		[148]
CaF_2	Impedance	0.80		5×10^{-4}	500		[80]
CaF_2	^{19}F NMR	0.33					[79]

[a] IGC processed.
[b] Chemically processed.

The spin–lattice relaxation rate T_1^{-1} of specific nuclei is sensitive to fluctuations of magnetic dipolar fields and electric field gradients around these nuclei. These fluctuations are induced by the movement of atoms or ions in the solid and are characterized by the autocorrelation function

$$G(t) = \overline{\langle m|\mathcal{H}_1(t_0)|k\rangle\langle k|\mathcal{H}_1(t_0+t)|m\rangle} \tag{19}$$

of the transition matrix element between two spin states [134]. Here $|m\rangle$ and $|k\rangle$ are spin states in the magnetic field B_0 (in the simplest case of a nucleus with spin $I = 1/2$ these are the states 'spin up' and 'spin down') and $\mathcal{H}_1$ is the perturbation Hamiltonian created by the time-dependent electromagnetic fields. The Fourier transform of $G(t)$ yields the spectral density

$$J(\omega) = \int_{-\infty}^{\infty} G(t)\, e^{-i\omega t}\, dt \tag{20}$$

of fluctuations of internal magnetic fields and electric field gradients at the site of the nuclear spins. Its values at and near the Larmor frequency ω_L determine the spin–lattice relaxation rate and we roughly have [133]

$$T_1^{-1} \propto J(\omega_L). \tag{21}$$

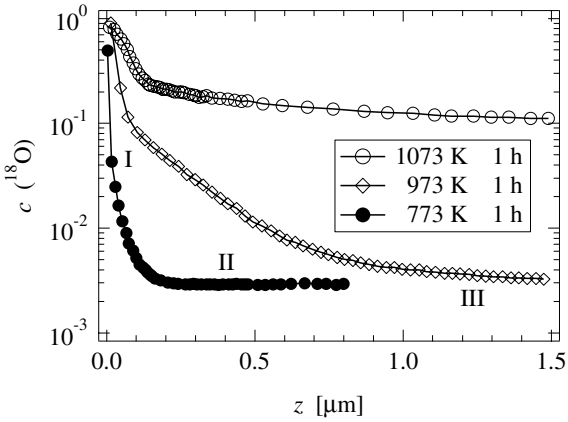

Figure 10. ^{18}O diffusion profiles in nanocrystalline ZrO_2 tempered at temperatures of 773, 973 and 1073 K for 1 h, after [147, 149, 150].

The model of Bloembergen, Purcell and Pound (BPP) [132] assumes isotropic, uncorrelated hopping of the nuclei which results in an exponential decay of the correlation function

$$G(t) = G(0)\exp(-|t|/\tau_c) \tag{22}$$

with the correlation time τ_c.

Equation (20) then yields a Lorentzian shaped spectral density

$$J(\omega) = G(0)\frac{2\tau_c}{1+(\omega\tau_c)^2}. \tag{23}$$

τ_c can be identified with the mean residence time τ of the atoms (apart from a factor of the order of unity, see, e.g., [135]). Thus T_1^{-1} measured as a function of temperature T at a given magnetic field B_0, i.e. Larmor frequency ω_L, passes through a maximum when

$$\omega_L\tau \approx 1. \tag{24}$$

This gives access to $\tau(T)$ and, via equation (16), to τ_0 and E_A. If the jump length ℓ and the dimensionality d of the diffusion process are known the diffusion coefficient D^{uc} of uncorrelated motion can be estimated using equation (6b).

6. Experimental results

6.1. Overview

In this chapter we present selected experimental results of diffusion measurements in nanocrystalline ceramics based on the experimental methods introduced in sections 5.2–5.5, namely SIMS, impedance spectroscopy and NMR spectroscopy. The investigated materials comprise classic oxygen conductors like ZrO_2, Li ion conductors, e.g. Li_2O, and the anion conductor CaF_2. The results are summarized in table 2 listing activation energies E_A as well as some diffusion coefficients D and dc conductivities σ_{dc}, respectively, at a representative temperature T. The table is subdivided into three main groups, corresponding to whether diffusion in the material is mainly due to Li, O or F ions. It is noticed that the activation energy derived from NMR relaxation measurements is always smaller than that of the dc conductivity for the same material. As mentioned in section 5.4 this is because NMR relaxation is sensitive to single ion hops, i.e. the short-range motion of the ion, whereas the dc conductivity probes

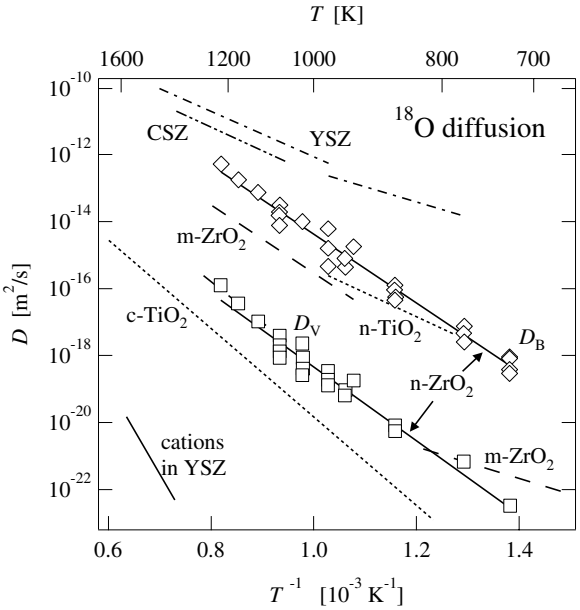

Figure 11. Tracer diffusion coefficients of ^{18}O determined by SIMS profiling for various micro- and nanocrystalline oxides: coarse grained titania c-TiO_2 (- - - -), nanocrystalline titania n-TiO_2 (- - - -), microcrystalline zirconia m-ZrO_2 (– – –), zirconia doped with yttrium or calcium (YSZ — · · —, CSZ — · —), bulk diffusion D_V (□) and interface diffusion D_B (◇) in nanocrystalline ZrO_2 (——), after [147].

the long-range transport. Furthermore there is a discrepancy between the activation energy of TiO_2 measured by SIMS and dc conductivity, respectively. This may be ascribed to the fact that, according to [148], the conductivity is borne mainly by Ti interstitials.

6.2. Tracer diffusivity

As a first example for measurements by a macroscopic method, figure 10 shows ^{18}O tracer diffusion profiles for pure nanocrystalline monoclinic ZrO_2 [147] recorded by SIMS. The powders were prepared by IGC. Samples with a relative mass density of 97% and an average crystallite size of 80 nm were obtained by *in situ* consolidation at ambient temperature under a pressure of 1.8 GPa and subsequent pressureless sintering at 950 °C. The profiles, which were recorded after diffusion annealing at three different temperatures, exhibit three distinct diffusion regimes (figure 10). These are attributed to diffusion in the crystalline bulk material (I), diffusion in the interfaces (II) and diffusion into the interior of the sample due to residual pores (III) [149]. The interface diffusivity is found to be 3–4 orders of magnitude higher than the volume diffusivity.

A comparison of the ^{18}O diffusivity in ZrO_2 with that in several other oxide ceramics is shown in figure 11 [147, 149]. It is remarkable that diffusion coefficients down to 10^{-22} m^2 s^{-1} are accessible. In nanocrystalline TiO_2 and ZrO_2 oxygen diffusion is enhanced by several orders of magnitude compared to that in the coarse grained materials. For nanocrystalline ZrO_2 both the volume diffusion coefficient D_V and the interface diffusion coefficient D_B are displayed. These were discriminated via the different regimes in the diffusion profiles. Such a discrimination between fast and slow diffusors was also possible by radiotracer measurements on nanocrystalline iron–nickel alloys [60, 151].

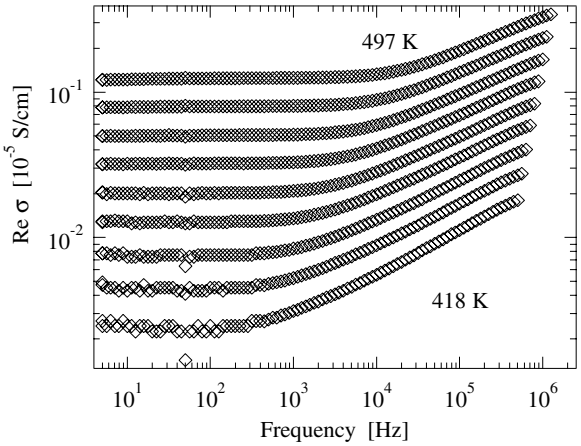

Figure 12. Conductivity spectra of nanocrystalline Li_2O at various temperatures in the range from 418 to 497 K [139].

6.3. Conductivity

6.3.1. Single-phase systems. Most studies concerning ionic conductivity in single-phase nanocrystalline ceramics were done on the classic oxide systems TiO_2 [148, 152, 153], CeO_2 [144, 153–157], ZnO [143, 158], yttrium-stabilized zirconia ZrO_2 (Y_2O_3) [142] and $(CeO_2)_{1-x}(BiO_{1.5})_x$ [145]. These materials are interesting for applications in fuel cells, sensors and as catalysts. Recently also the ionic conductivity in nanocrystalline Li ion conductors, e.g. Li_2O [139] or $LiBO_2$ [138], was measured. Li ion conducting materials are extensively used in Li batteries [159]. Investigation of nanocrystalline Li conductors may give access to advanced electrolytes or electrode materials [160, 161] in battery systems. Complementary to impedance, in these materials Li diffusion can conveniently be studied by ^{7}Li NMR relaxation techniques, see section 5.5. Another nanocrystalline single-phase system, which was one of the first studied by impedance spectroscopy, is the anion conductor CaF_2 [80, 162].

As an example, figure 12 shows conductivity spectra of nanocrystalline Li_2O [139]. It was prepared by ball milling of the coarse grained source material for 16 h, resulting in an average grain size of about 20 nm (cf figure 5). The spectra show the typical behaviour found in many ionic conductors. At low frequencies the spectra display a distinct plateau which represents the dc conductivity σ_{dc} of the material. The temperature dependence of the dc conductivity yields an activation energy of about 0.9 eV, which refers to the long-range transport of the charge carriers, i.e. the Li ions. At higher frequencies the spectra exhibit a strongly dispersive region due to the correlated motion of Li ions on short time scales.

An example where bulk and interface contributions to the overall impedance were discriminated is presented in figure 13. It shows the impedance plot at 550 K of nanocrystalline zirconia stabilized with Y_2O_3 which was produced by IGC, resulting in an average grain diameter of about 50 nm [142]. Two arcs can be discerned which can be assigned to the bulk material (high frequency arc) and to the grain boundaries. At low frequencies contributions due to the electrodes are visible. From measurements at various temperatures the activation energy for bulk and grain boundary conduction, respectively, was obtained (figure 14). In the present case the conductivity is higher and the activation energy is lower in the bulk material than in the grain boundaries. However, in both cases the values are in the same range as those for microcrystalline samples obtained from the literature.

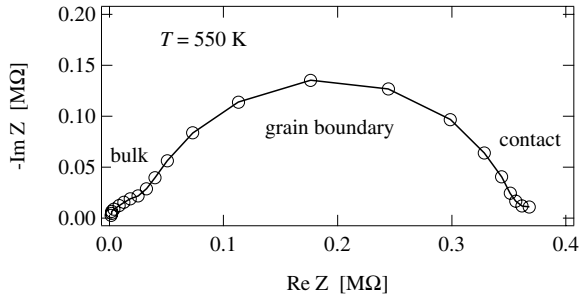

Figure 13. Impedance plot of nanocrystalline yttrium stabilized zirconia at 550 K, after [142].

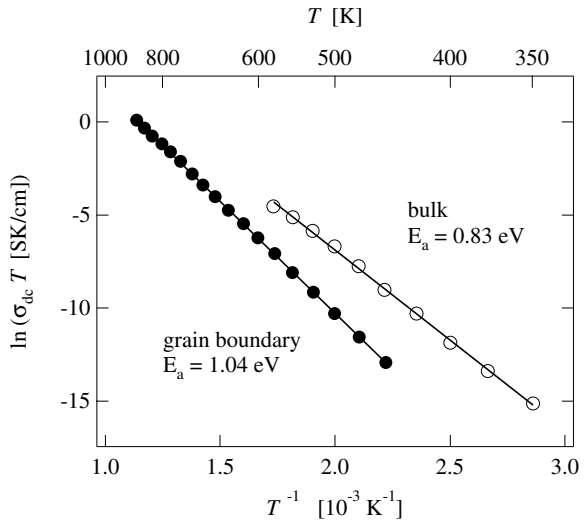

Figure 14. Grain boundary and bulk conductivities of nanocrystalline yttrium stabilized zirconia, after [142].

In contrast to the above, for nanocrystalline CaF_2 the overall conductivity was found to be enhanced by four orders of magnitude as compared to the single-crystalline material [162]. CaF_2 is a model substance for anionic conduction. The nanocrystalline material was prepared by IGC. High resolution TEM studies revealed an average crystallite size of 9 nm (cf figure 4). The enhanced conductivity in the nanocrystalline material (figure 15) was explained by the formation of ionic space charge regions at the grain boundaries [40, 80]. These space charge layers have a thickness of the order of the Debye length λ, which is inversely proportional to the square root of the concentration of ionic defects, and results in a high conductivity *parallel* to the interfaces. In the present case λ (about 1 nm) is much smaller than the average grain size. The enhancement of the overall conductivity is caused by the high number of interfaces and can quantitatively be described by the space charge model (figure 15). It should be noted that diffusion *across* a grain boundary can be either suppressed or not, depending on the type of grain boundary, as was shown by an oxygen diffusion study on single-grain boundaries in $SrTiO_3$ bicrystals [163].

As discussed above there can be more than one charge carrier contributing to the overall conductivity. Discrimination can be done via electrodes blocking the charge carriers

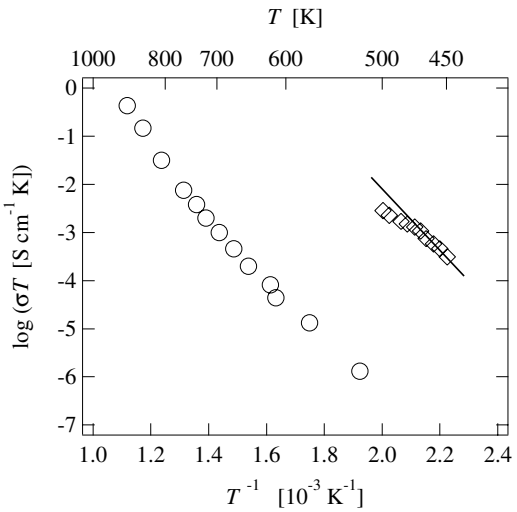

Figure 15. The conductivity of nanocrystalline CaF_2 (◇) compared to that of the microcrystalline material (○). The line represents the estimated conductivities assuming a pronounced space charge effect at the grain boundaries, after [80].

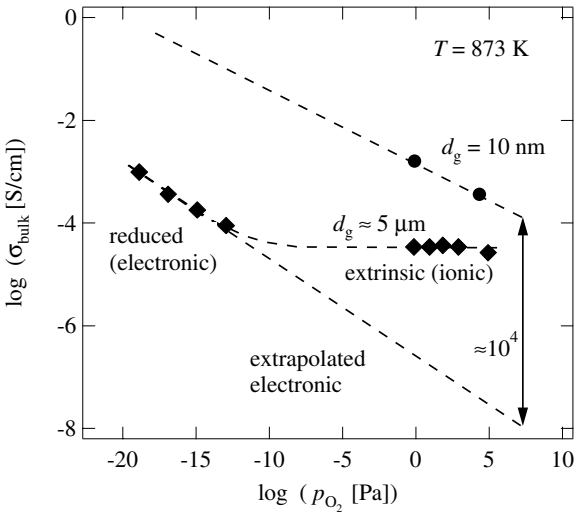

Figure 16. Oxygen partial pressure dependence of the conductivity of micro (◆)- and nanocrystalline (●) CeO_{2-x}, after [144].

selectively [118, 164]. Another possibility is to compare conductivity measurements with tracer diffusion measurements. The Haven ratio H_R can indicate whether more than one charge carrier is involved in the overall conductivity or not (section 4). A further possibility, for oxygen conductors, is to study the oxygen partial pressure dependence of the conductivity. An example is shown in figure 16 for the mixed conducting material CeO_{2-x} [144, 153, 155–157]. The conductivity of the micro- and nanocrystalline materials is displayed for an oxygen partial pressure range covering about 25 decades. For the microcrystalline material two regimes are found. At low oxygen partial pressures the conductivity decreases with increasing partial

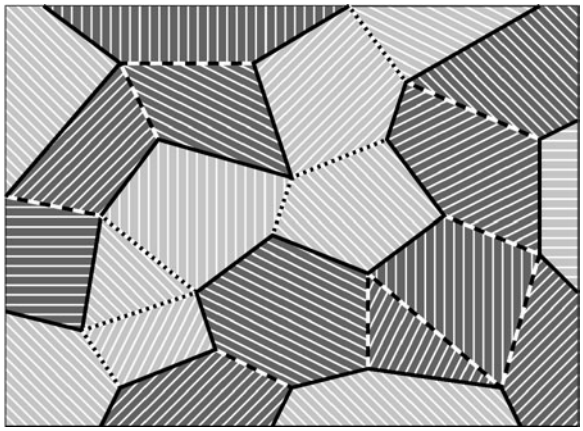

Figure 17. Sketch of a composite material of ionic conductor grains (light grey areas) and insulator grains (dark grey areas). The network of interfaces consists of interfaces between ionic conductor grains (dotted lines), interfaces between insulator grains (broken lines) and interfaces between ionic conductor and insulator grains (full lines).

pressure, revealing predominantly electronic conduction [165]. For higher oxygen partial pressures the conductivity is governed by ionic conduction resulting in a plateau. Comparison of the extrapolated electronic contribution in the microcrystalline material with the electronic conductivity in the nanocrystalline material shows that the latter is enhanced by about four orders of magnitude. So the ratio of the electronic to the ionic conductivity (and thus the transference number) is drastically changed by variation of the grain size, at least at higher oxygen partial pressures. The enhanced electronic conductivity is attributed to an increased nonstoichiometry in the nanocrystals.

6.3.2. Composites. In composite materials new effects may occur due to the interfaces between the different components. Figure 17 shows a sketch of a composite material consisting of ion conducting crystallites (light grey areas) and insulating grains (dark grey areas). Instead of one there are now three types of interfaces. These are interfaces between the ionic conductor grains (dotted lines), between the insulator grains (broken lines) and between the ionic conductor and the insulator grains (full lines). The latter can lead to surprising effects in the conductivity of composite materials. Liang [166] discovered for the composite LiI:Al_2O_3 that, when the insulator Al_2O_3 is added to the Li ion conductor LiI, the overall conductivity of the material increases (figure 18). This is explained by an enhanced conductivity in the interfacial regions between the ionic conductor grains and the insulator grains. Such systems are called dispersed ionic conductors (DIC). Conventionally, these have been composites of microcrystalline materials, partly with sub-micron insulator grains. The conductivity enhancement in the interfacial regions may have different origins, e.g. the formation of space charge layers, an enhanced concentration of dislocations or the formation of new phases [38, 167–169]. The highly conducting interfaces can lead to a pronounced maximum in the total ionic conductivity as a function of the insulator content which can be described by percolation of these interfaces [170–172]. Similar results were found for the composite material CuBr:TiO_2 [173–175]. It gives a first hint that the grain size of the ionic conductor plays a role. CuBr with an average grain size of 3 μm shows a greater enhancement than that with 5 μm (see figure 19).

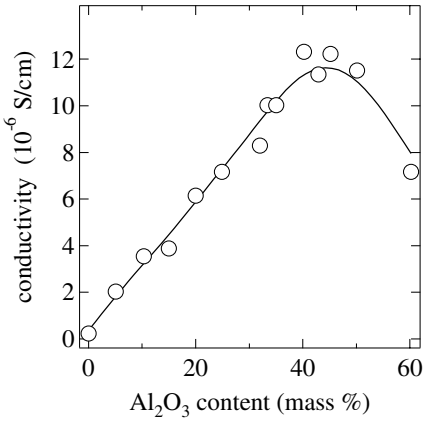

Figure 18. Conductivity of LiI:Al_2O_3 composites, after [166].

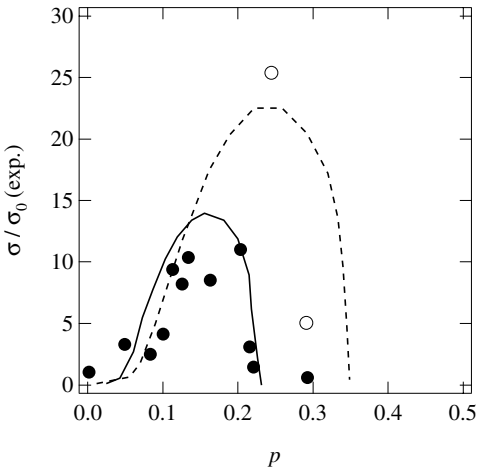

Figure 19. Conductivity of CuBr:TiO_2 composites, normalized to that of pure CuBr (σ_0), versus insulator volume fraction p, after [173, 174]. The grain size of CuBr was 5 μm (●) and 3 μm (○), respectively. The full and broken curves show results from a resistor network model.

A system where both the average grain size of the ionic conductor and of the insulator were varied from 10 μm to 20 nm is Li_2O:B_2O_3 [139]. Results are displayed in figure 20. Microcrystalline and nanocrystalline pure Li_2O have similar conductivities. However, when the insulator is added the two forms behave quite differently. In the microcrystalline material the conductivity decreases monotonically with insulator content and becomes smaller than 10^{-9} S cm^{-1}, the detection limit of the experimental set-up, for $x \geqslant 0.5$. For the nanocrystalline counterpart the conductivity increases up to a maximum at $x \approx 0.5$, then decreases and becomes smaller than 10^{-9} S cm^{-1} for $x \geqslant 0.95$. An alternative way to look at the data in figure 20 is to start from the pure nanocrystalline insulator ($x = 1$) and to note that the admixture of a few per cent of the nanocrystalline ionic conductor increases the conductivity by a factor of more than 10 over the value for the pure conductor ($x = 0$), whereas the corresponding microcrystalline system reaches its maximum conductivity only for the pure conductor. All these characteristics could be reproduced by a continuum percolation model, represented by the broken curves in figure 20, which assumes an enhanced conductivity in the

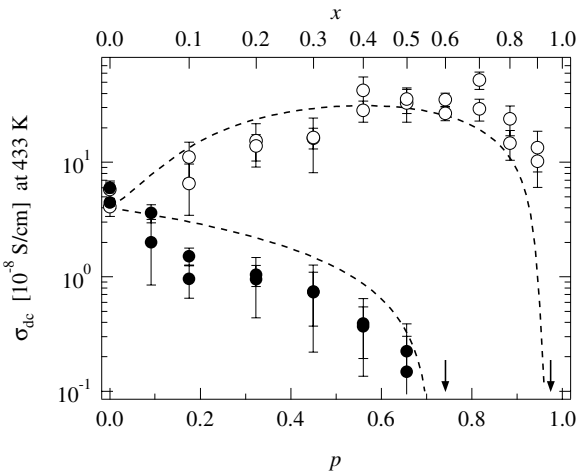

Figure 20. Conductivity versus insulator volume content p for (●) micro- and (○) nanocrystalline $(1-x)Li_2O{:}xB_2O_3$ composites at 433 K, after [139]. The upper abscissa shows the insulator mole fraction x. For all compositions two independent samples were prepared and investigated. The arrows indicate that further measurements have been done for $x > 0.5$ for the microcrystalline composites and for $x > 0.9$ for the nanocrystalline samples, respectively, and that the dc conductivity decreases drastically above those thresholds and falls below the detection limit of our apparatus. The broken curves represent results of a continuum percolation model assuming an enhanced conductivity in the interfacial regions between ionic conductor (Li_2O) and insulator (B_2O_3).

interfaces between the two materials. The thickness of this interface (1 nm) was supposed to be independent of the grain size [44]. As a result there is no conductivity enhancement in the microcrystalline case where the volume fraction of the interfaces is negligible.

For nanocrystalline CaF_2 it was assumed above (section 6.3.1) that the conductivity enhancement was caused by the formation of space charge layers at the grain boundaries. Maier and coworkers [176] have investigated the influence of such interfacial effects in layered CaF_2–BaF_2 heterostructures, grown by molecular beam epitaxy, with layer thicknesses in the nanometre regime (figure 21). They found that the conductivity in these packages parallel to the layers is enhanced compared to that of the pure CaF_2 and BaF_2 films. The thinner the layers the larger the enhancement of the conductivity is. As shown by the following arguments (cf figure 21), this is due to the formation of ionic space charge layers. Because all films have a similar total thickness L of about 500 nm, samples with thinner layers comprise more interfaces. In the inset of figure 21 the conductivity is plotted versus the number of interfaces per unit length (N/L). For distances of the interfaces larger than 50 nm (corresponding to $N/L < 0.2 \times 10^{-6}$ cm^{-1}) the conductivity is proportional to the number of interfaces. When the distance of the interfaces becomes smaller than 50 nm and thus falls below the order of magnitude of the Debye length in this system, the ionic space charge layers of neighbouring interfaces overlap, which leads to an even stronger enhancement of the conductivity. At this point, the single interfaces lose their individuality and an artificial ionically conducting material with anomalous transport properties is generated.

6.4. NMR lineshape

As pointed out in section 5.1, NMR relaxation spectroscopy can give microscopic access to the diffusion of ions. In this section we present results for nanocrystalline Li ion conductors

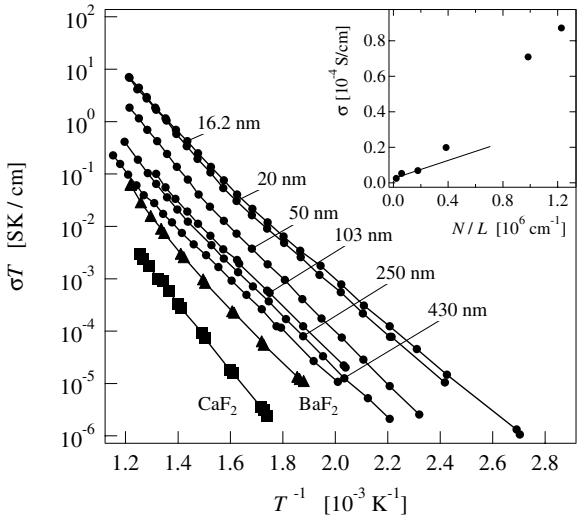

Figure 21. Conductivity of CaF_2–BaF_2 layered heterostructures parallel to the films for different layer thicknesses compared to the pure materials with the same total thickness L. The inset shows the conductivity of the heterostructures at 320 °C rising with the number of interfaces per unit length N/L, after [176].

from ^{7}Li NMR lineshape studies [140, 177]. Figure 22 displays ^{7}Li NMR lineshapes of different micro- and nanocrystalline composites $(1-x)Li_2O{:}xB_2O_3$ at 433 K and a central frequency of 58 MHz. The microcrystalline composites with $x = 0$ and 0.5 (figures 22(a) and (b)) exhibit only one broad line without structure, which is typical of homogeneous solids at low temperatures in the rigid-lattice regime (cf section 5.4). Due to the tetrahedral symmetry of the Li sites in Li_2O no quadrupole satellites are to be expected. In contrast to the microcrystalline samples the nanocrystalline ones show two contributions to the NMR line at 433 K (figures 22(c) and (d)). These are a broad component which has a similar linewidth as the line of the microcrystalline material and a motionally narrowed component at the same central frequency.

The variation of the lineshapes with temperature (not displayed) reveals that below 350 K the nanocrystalline samples also show only one broad line. For the microcrystalline samples the line is narrowed homogeneously at temperatures above 450 K. For the nanocrystalline samples the motional narrowing takes place in two steps. At temperatures above 350 K one part of the line is narrowed, resulting in the lineshape shown for 433 K in figures 22(c) and (d). At temperatures beyond 450 K the rest of the line is also narrowed. Thus the broad component represents the immobile Li ions inside the nanocrystalline grains and the narrow component represents more mobile Li ions which are located in the interfacial regions.

An evaluation of the lineshapes is shown in figure 23. The two components of the lineshapes for the nanocrystalline composites can be fitted with a sum of two Gaussian functions (figure 23(a)). Plotting both linewidths versus temperature (figure 23(b)) one notices that motional narrowing of the broad component sets in at about 450 K while narrowing of the other component is already completed at 350 K. The area fraction A_f of the narrow component corresponds to the number fraction of fast Li ions. As long as the broad component does not show motional narrowing, i.e. below about 450 K, A_f is equal to the number fraction of Li ions in the interfacial regions, from which an effective volume fraction of interfacial regions can be estimated. This is shown in figure 23(c) for the nanocrystalline composites with $x = 0$ and 0.5.

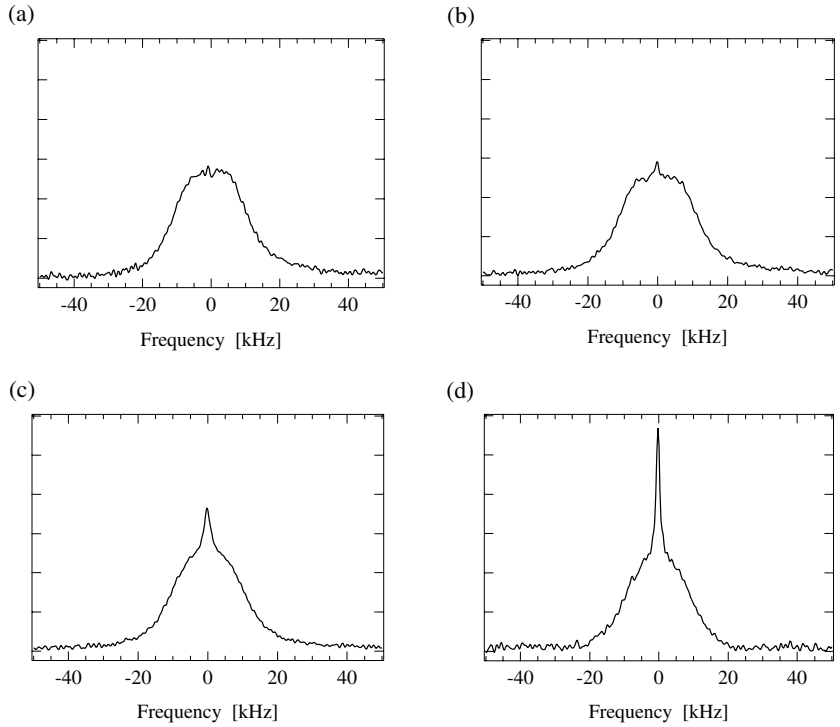

Figure 22. ^{7}Li NMR lineshapes at 58 MHz and 433 K of (a) microcrystalline Li_2O, (b) microcrystalline $(1-x)Li_2O{:}xB_2O_3$, $x = 0.5$, (c) nanocrystalline Li_2O, (d) nanocrystalline $(1-x)Li_2O{:}xB_2O_3$, $x = 0.5$ [140].

In the composite material with $x = 0.5$ the number fraction of fast Li ions is significantly higher than in pure nanocrystalline Li_2O in the relevant temperature range up to about 450 K. This is ascribed to the interfaces between unlike crystallites and consistent with the conductivity increase reported in section 6.3.2.

Similar lineshapes were also found for ^{7}Li in nanocrystalline $Li_2O{:}Al_2O_3$ [141] and for ^{7}Li (central NMR transition) in nanocrystalline $LiNbO_3$ [136, 178] and Li_xTiS_2 [137, 179, 180] as well as in their microcrystalline counterparts. In the case of $LiNbO_3$ [130] and Li_xTiS_2 [137] the amorphous modifications were also investigated for comparison. Here the ^{7}Li NMR lineshapes show only *one* contribution over the total range of motional narrowing. This is because, in contrast to the nanocrystalline materials, the amorphous modifications have a *homogeneously* disordered structure with only one species of Li ions.

Historically, discrimination of differently mobile ions in nanocrystalline ceramics by NMR lineshape studies was first achieved for ^{19}F in nanocrystalline CaF_2 [79, 101].

6.5. NMR spin–lattice relaxation rate

Besides NMR lineshape the first NMR spin–lattice relaxation study of diffusion in a nanocrystalline ceramic was also performed on ^{19}F in CaF_2 [79]. In the following we confine ourselves again to results on Li ion conductors. An example for ^{7}Li NMR relaxation rates is given in figure 24 for micro- and nanocrystalline $LiNbO_3$ [136, 181]. Using the special technique of measuring spin–lattice relaxation rates in the pulsed rotating frame [182],

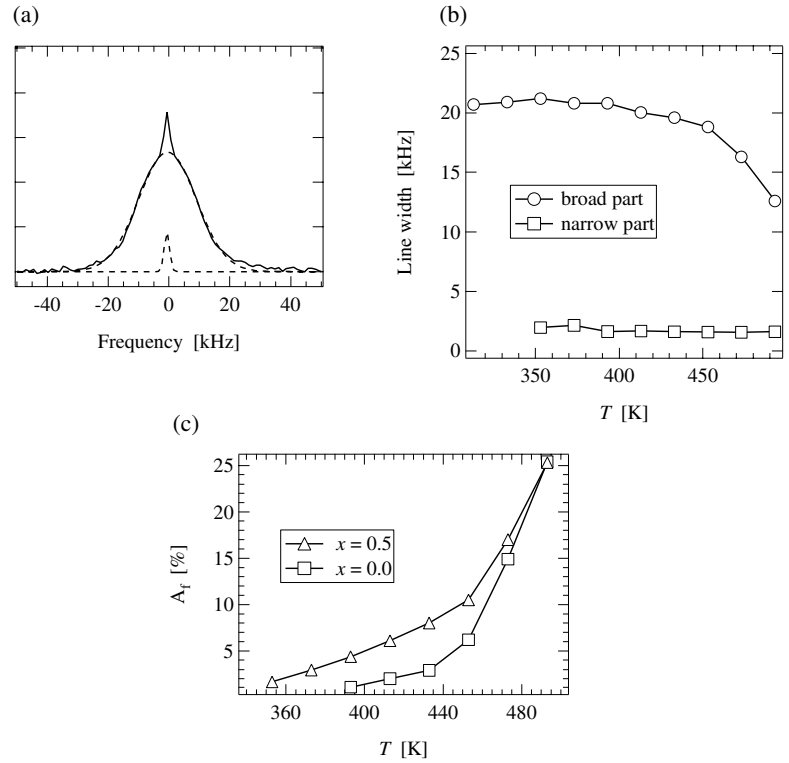

Figure 23. (a) ^{7}Li NMR lineshape for nanocrystalline Li_2O at 58 MHz and 433 K. (b) The linewidths of the two components in nanocrystalline Li_2O versus temperature. (c) The area fraction of the narrow component of the ^{7}Li NMR lineshapes for nanocrystalline $(1-x)Li_2O{:}xB_2O_3$ composites with $x = 0$ and 0.5, respectively, versus temperature [177].

$T_{1e}^{-1}(T)$ was measured at different frequencies (figure 24(a)). The figure shows the typical behaviour of the diffusion-induced spin–lattice relaxation rate according to a modified BPP ansatz (cf equation (23)). Characteristic features are the maximum in the temperature dependence of the relaxation rate, a high-temperature flank with no frequency dependence and a low-temperature flank with $T_1^{-1} \propto \omega_L^{-\beta}$, where $\beta = 2$ in the standard BPP case. Here $\beta = 1.5$ is found which is an indication of correlated motion, which can be explained by the combined effect of structural disorder and Coulomb interaction [183]. Figure 24(b) shows the ^{7}Li spin–lattice relaxation rate T_1^{-1} in the laboratory reference frame for nanocrystalline $LiNbO_3$ in comparison with the results for the microcrystalline sample. At low temperatures (<500 K for microcrystalline and <200 K for nanocrystalline $LiNbO_3$) a background relaxation rate being scarcely dependent on temperature is found. At higher temperatures the low-temperature flank of the diffusion-induced peak is visible and its slope yields an activation energy of about 0.75 eV for the microcrystalline and 0.27 eV for the nanocrystalline sample. Furthermore, the flank is shifted to lower temperatures in the nanocrystalline material. Both facts indicate faster diffusion in nanocrystalline $LiNbO_3$. Interestingly, amorphous $LiNbO_3$ [130] yields similar diffusion parameters. So, judging from the Li dynamics, the interfacial regions in the nanocrystalline material, prepared by high-energy ball milling, seem to be of an amorphous-like structure. This was recently corroborated by EXAFS measurements on identical samples which showed that roughly 50% of the material is amorphous [184].

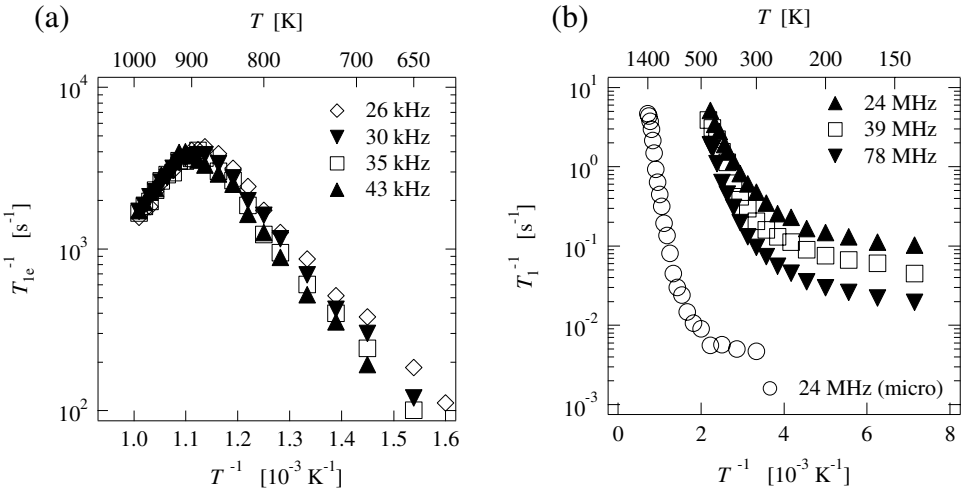

Figure 24. (a) ^{7}Li spin–lattice relaxation rate of ^{7}Li (in the pulsed rotating frame, T_{1e}^{-1}) versus inverse temperature for microcrystalline $LiNbO_3$ at various frequencies. (b) Spin-lattice relaxation rate in the laboratory reference frame (T_1^{-1}) versus inverse temperature at various frequencies for nanocrystalline $LiNbO_3$. For comparison, results for the microcrystalline sample at 24 MHz are displayed, too, after [136, 181].

A comparative T_1^{-1} study of the nanocrystalline (average grain size about 12 nm) with the microcrystalline and the amorphous forms was also performed for Li_xTiS_2, see figure 25 [137, 179, 180]. The crystalline modification of Li_xTiS_2 used here is the well-known hexagonal phase [185]. This is a layered structure leading to two-dimensional fast diffusion of the intercalated Li ions [104]. The activation energy for single ion jumps in nanocrystalline Li_xTiS_2 (0.16 eV) is not significantly smaller than that in the microcrystalline material (0.19 eV) and larger than in the amorphous one (0.07 eV). This indicates that the diffusion pathways in the two crystalline forms are similar and determined by the layer structure of the grains while in the amorphous phase the less dense packing may be responsible for the reduction of the activation energy. The spin–lattice relaxation rate measured after annealing a freshly prepared nanocrystalline Li_xTiS_2 sample at various temperatures was also used to study the kinetics of the Li intercalation [137].

In nanocrystalline Li_2O two Li species having different mobilities were discriminated via their different relaxation rates T_1^{-1} which showed up in biexponential magnetization transients [140]. This contrasts with the results for microcrystalline Li_2O where relaxation is monoexponential. It was found that T_1^{-1} of the slower Li species in nanocrystalline Li_2O is similar to T_1^{-1} in microcrystalline Li_2O. Therefore the slower Li species has to be attributed to the crystalline grains whereas the faster Li ions are located in the interfacial regions of the nanocrystalline material. These results are consistent with the lineshape analysis presented in section 6.4 (cf figure 22) which in turn reveals two different spin–spin relaxation rates T_2^{-1}.

The activation energies of the two species in nanocrystalline Li_2O were found to be similar and agree with that of the microcrystalline material. This may be explained by the formation of ionic space charge layers being located in the ionic conductor in the vicinity of the interfaces. This results in an increased concentration of point defects, i.e. charge carriers. The type of point defects, in the present case vacancies in the Li sublattice, is unchanged and therefore the activation energy is the same for the nano- and the microcrystalline material. Adding the insulator B_2O_3 does not influence the activation energy whereas the number fraction of

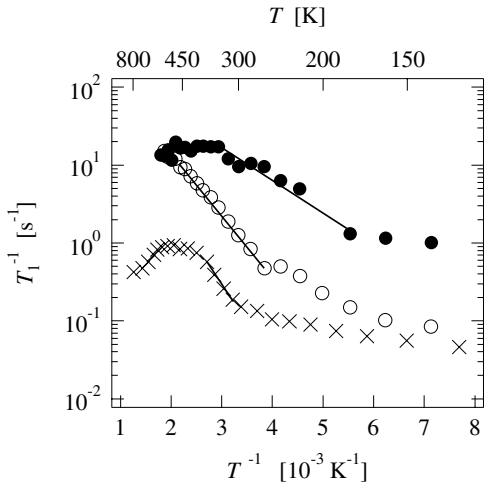

Figure 25. ^{7}Li spin–lattice relaxation rates T_1^{-1} in microcrystalline (×), nanocrystalline (○) and amorphous (●) Li_xTiS_2 ($x \approx 2/3$) versus inverse temperature at 24.5 MHz. The lines indicate slopes from which activation energies were estimated, after [137].

fast Li ions is increased in the nanocrystalline material. So the interfaces between unlike crystallites (Li_2O and B_2O_3) seem to generate more fast Li ions than the interfaces between Li_2O crystallites. This also leads to stronger deviations from monoexponential relaxation behaviour in the nanocrystalline composite Li_2O:B_2O_3 than in pure nanocrystalline Li_2O. Figure 26 shows Arrhenius plots of the discriminated relaxation rates of the fast and slow Li ions in nanocrystalline $(1-x)Li_2O$:xB_2O_3, $x = 0.5$, together with T_1^{-1} data of the microcrystalline counterpart. The activation energies are in the range (0.32 ± 0.04) eV.

Results are very similar for the analogous system Li_2O:Al_2O_3 [141]. This suggests that the special type of insulator added to the Li_2O is not important and that the increase of the conductivity found in the impedance measurements (see section 6.3.2) reveals a rather generic behaviour.

7. Conclusions

Nanocrystalline or other nanostructured materials with a large volume fraction of interfacial regions often show new properties concerning diffusion and ionic conduction. Experimental results, mainly for lithium, oxygen and fluorine ion conducting nanocrystalline ceramics, studied so far by essentially three methods out of those surveyed in section 5.1, have been listed in table 2. As an example for a macroscopic method, SIMS has enabled investigations of long-range diffusion profiles where it has been possible to discriminate between contributions from crystallites, grain boundaries and residual pores. Impedance spectroscopy also allowed a differentiation between ionic conduction in grain boundaries and crystallites due to their different time scales of electrical relaxation. As far as microscopic methods are concerned, NMR relaxation techniques have proven once more to be valuable tools for the investigation of dynamic phenomena on short time scales. Since NMR spectroscopy is thus sensitive to short range motion of specific atoms and, on the other hand, SIMS and impedance spectroscopy probe the long range transport, these methods help to relate the micro- or nanostructure of the materials to their macroscopic diffusion behaviour. Using static NMR lineshape studies it was possible to

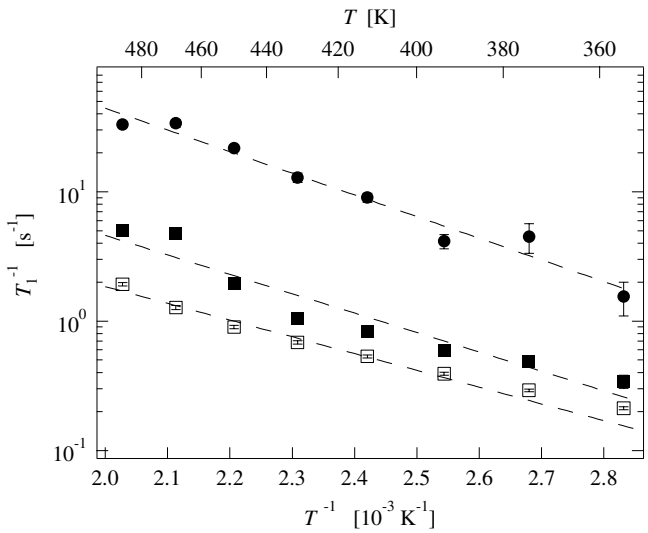

Figure 26. ^{7}Li spin–lattice relaxation rates in nano- and microcrystalline $(1-x)Li_2O{:}xB_2O_3$, $x = 0.5$, versus inverse temperature at 58 MHz. In the nanocrystalline material two Li species could be discriminated via their different ^{7}Li spin–lattice relaxation rates T_1^{-1} (full symbols) which differ by about one order of magnitude, resulting in biexponential magnetization transients. The species with the lower rates (■) shows similar rates as the microcrystalline material (□) and is identified with less mobile Li ions inside the crystallites whereas the faster relaxing, and thus faster moving, Li ions (●) are located in the interfacial regions. The broken lines represent Arrhenius fits, after [140].

verify the heterogeneous structure of nanocrystalline materials consisting of crystalline grains and interfacial regions. This contrasts with the structure in microcrystalline materials appearing to be homogeneous when studied with NMR techniques due to the small volume fraction of interfaces. The temperature dependence of these lineshapes as well as NMR spin–lattice relaxation spectroscopy show that the heterogeneous structure in the nanocrystalline materials results in a heterogeneous dynamic behaviour with two different species of, for example, Li ions. These are relatively slow ions in the ordered grains and fast ions in the structurally disordered interfacial regions. This again differs from the microcrystalline materials where only one species of mobile ions, that in the grains, is observed.

Diffusion and ionic conduction in nanocrystalline ceramics is far from being understood completely. This is mainly due to the lack of knowledge about the detailed microstructure in these materials which is generally even less well known than that of nanocrystalline metals. The complexity of these systems is determined, for example, by the number of phases involved, the variety of defect species, the deviation from purely cationic or anionic conduction, the average grain size and the width of the grain size distribution. In future studies, as an example, the influence of the preparation method should be investigated in more detail. Nanocrystalline powders prepared by different methods having the same average grain size may have different macroscopic properties since the degree of structural disorder in the interfaces may be different, e.g. ball milling leads to interfaces which are partially amorphous for some materials.

In any case the combination of long range and short range diffusion techniques is essential for a comprehensive understanding of the structure–diffusion relations which in turn is a prerequisite to tailor functional materials with optimized properties.

Acknowledgments

We are grateful to the Deutsche Forschungsgemeinschaft for financial support. PH would also like to acknowledge financial help by the Fonds der Chemischen Industrie.

References

[1] Karch J, Birringer R and Gleiter H 1987 *Nature* **330** 556–8
[2] Yip S 1998 *Nature* **391** 532–3
[3] Baller J, Krüger J K, Birringer R and Proust C 2000 *J. Phys.: Condens. Matter* **12** 5403–9
[4] Betz U and Hahn H 1999 *Nanostruct. Mater.* **12** 911–14
[5] Tuller H L 1997 *J. Electroceram.* **1** 211–18
[6] George A M, Íñiguez J and Bellaiche L 2001 *Nature* **413** 54–7
[7] Demetry C and Shi X 1998 *Solid State Ion.* **118** 271–9
[8] Nan C-W, Holten S, Birringer R, Gao H, Kliem H and Gleiter H 1997 *Phys. Status Solidi* a **164** R1–2
[9] Wittmer H, Holten S, Kliem H and Breuer H D 2000 *Phys. Status Solidi* a **181** 461–9
[10] Mamiya H, Nakatani I and Furubayashi T 1998 *Phys. Rev. Lett.* **80** 177–80
[11] Jonsson T, Mattsson J, Djurberg C, Khan F A, Nordblad P and Svedlindh P 1995 *Phys. Rev. Lett.* **75** 4138–41
[12] Stewart S J, Borzi R A, Punte G, Mercader R C and Garcia F 2001 *J. Phys.: Condens. Matter* **13** 1743–57
[13] Garcia-Otero J, Porto M, Rivas J and Bunde A 2000 *Phys. Rev. Lett.* **84** 167–70
[14] Chen J P, Sorensen C M, Klabunde K J and Hadjipanayis G C 1995 *Phys. Rev.* B **51** 11527–32
[15] Zhang D, Klabunde K J, Sorensen K J and Hadjipanayis G C 1998 *Phys. Rev.* B **58** 14167–70
[16] Weller H, Schmidt H M, Koch U, Fojtik A, Baral S, Henglein A, Kunath A, Weiss K and Dieman E 1986 *Chem. Phys. Lett.* **124** 557–60
[17] Peng X, Manna L, Yang W, Wickham J, Scher E, Kadavanich A and Alivisatos A P 2000 *Nature* **404** 59–61
[18] Shim M and Guyot-Sionnest P 2000 *Nature* **407** 981–3
[19] Nan C-W, Birringer R, Krauss W, Gao H and Gleiter H 1997 *Phys. Status Solidi* a **162** R3–4
[20] Schmechel R, Kennedy M, von Seggern H, Winkler H, Kolbe M, Fischer R A, Xaomao L, Benker A, Winterer M and Hahn H 2001 *J. Appl. Phys.* **89** 1679–86
[21] Linsebigler A L, Lu G and Yates J T Jr 1995 *Chem. Rev.* **95** 735–58
[22] Ying J Y and Sun T 1997 *J. Electroceram.* **1** 219–38
[23] Gleiter H 1989 *Prog. Mater. Sci.* **33** 223–315
[24] Weissmüller J and Ehrhardt H 1998 *Phys. Rev. Lett.* **81** 1114–17
[25] Jacob K T, Jayadevan K P, Mallya R M and Waseda Y 2000 *Adv. Mater.* **12** 440–4
[26] Atkinson A 1994 *Materials Science and Technology* vol 11, ed R W Cahn, P Haasen and E J Kramer (Weinheim: VCH) pp 295–337
[27] Würschum R, Brossmann U and Schaefer H-E 2002 *Nanostructured Materials—Processing, Properties, and Applications* ed C C Koch (Norwich: Noyes Publications) pp 267–99
[28] Würschum R 1999 *Rev. Metall.* **96** 1547–53
[29] Larikov L N 1995 *Met. Phys. Adv. Tech.* **15** 1–37
[30] Mishin Y and Herzig C 1995 *Nanostruct. Mater.* **6** 859–62
[31] Divinski S V and Larikov L N 1997 *Defect Diffus. Forum* **143–147** 1469–74
[32] Shackelford J F 1992 *Encyclopedia of Applied Physics* vol 3, ed G L Trigg (New York: VCH) pp 169–87
[33] Kingery W D, Bowen H K and Uhlmann D R 1976 *Introduction to Ceramics* (New York: Wiley)
[34] Cahn R W, Haasen P and Kramer E J (ed) 1994 *Materials Science and Technology* vol 11 (Weinheim: VCH)
[35] Chen I-W and Xue L A 1990 *J. Am. Ceram. Soc.* **73** 2585–609
[36] Schmalzried H 1995 *Chemical Kinetics of Solids* (Weinheim: VCH)
[37] Abrahamson J and Dinniss J 2000 *Nature* **403** 519–21
[38] Maier J 1995 *Prog. Solid State Chem.* **23** 171–263
[39] Chung Y-C, Kim C K and Wuensch B J 2000 *J. Appl. Phys.* **87** 2747–52
[40] Maier J 2000 *Solid State Ion.* **131** 13–22
[41] Maier J 2000 *Electrochemistry* **68** 395–402
[42] Damson B and Würschum R 1996 *J. Appl. Phys.* **80** 747–51
[43] Gleiter H 1992 *Phys. Status Solidi* b **172** 41–51
[44] Siegel R W 1994 *Encyclopedia of Applied Physics* vol 11, ed G L Trigg, E H Immergut, E S Vera and W Greulich (New York: VCH) pp 173–200
[45] Gleiter H 2000 *Acta Mater.* **48** 1–29

[46] Siegel R W and Hahn H 1987 *Current Trends in the Physics of Materials* ed M Yussouff (Singapore: World Scientific) pp 403–19
[47] Andrievski R A 1998 *Mater. Sci. Forum* **282/283** 1–9
[48] Winterer M 2002 *Nanocrystalline Ceramics—Synthesis and Structure* (Berlin: Springer)
[49] Weissmüller J 1996 *Nanomaterials: Synthesis, Properties and Applications* ed A S Edelstein and R C Cammarata (Bristol: Institute of Physics Publishing) pp 219–76
[50] Löffler J and Weissmüller J 1995 *Phys. Rev.* B **52** 7076–93
[51] Phillpot R S, Wolf D and Gleiter H 1995 *J. Appl. Phys.* **78** 847–61
[52] Phillpot R S, Wolf D and Gleiter H 1995 *Scr. Metall. Mater.* **33** 1245–51
[53] Keblinski P, Wolf D, Phillpot S R and Gleiter H 1999 *Scr. Mater.* **41** 631–6
[54] Stern E A, Siegel R W, Newville M, Sanders P G and Haskel D 1995 *Phys. Rev. Lett.* **75** 3874–7
[55] Van Swygenhoven H, Farkas D and Caro A 2000 *Phys. Rev.* B **62** 831–8
[56] Kaur I, Mishin Y and Gust W 1995 *Fundamentals of Grain and Interphase Boundary Diffusion* (New York: Wiley)
[57] Wolf D and Yip S (ed) 1992 *Materials Interfaces* (London: Chapman and Hall)
[58] Horváth J 1989 *Defect Diffus. Forum* **66–69** 207–28
[59] Peteline A, Peteline S and Oreshina O 2001 *Defect Diffus. Forum* **194–199** 1265–70
[60] Divinski S V, Hisker F, Kang Y-S, Lee J-S and Herzig C 2002 *Z. Metallk.* **93** 265–72
[61] Hahn H and Padmanabhan K A 1995 *Nanostruct. Mater.* **6** 191–200
[62] Mayo M J, Chen D-J and Hague D C 1996 *Nanomaterials: Synthesis, Properties and Applications* ed A S Edelstein and R C Cammarata (Bristol: Institute of Physics Publishing) pp 165–97
[63] Mayo M J 1996 *Int. Mater. Rev.* **41** 85–115
[64] Höfler H J, Hahn H and Averbach R S 1991 *Defect Diffus. Forum* **75** 195–210
[65] Siegel R W, Ramasamy S, Hahn H, Zongquan L and Ting L 1988 *J. Mater. Res.* **3** 1367–72
[66] Srdic V V, Winterer M, Miehe G and Hahn H 1999 *Nanostruct. Mater.* **12** 95–100
[67] Viswanath R N and Ramasamy S 1997 *Nanostruct. Mater.* **8** 155–62
[68] Natter H, Schmelzer M, Janßen S and Hempelmann R 1997 *Ber. Bunsenges. Phys. Chem.* **101** 1706–13
[69] Zarur A J and Ying J Y 2000 *Nature* **403** 65–7
[70] Härtl W, Beck Ch, Roth M, Meyer F and Hempelmann R 1997 *Ber. Bunsenges. Phys. Chem.* **101** 1714–17
[71] Fecht H J 1995 *Nanostruct. Mater.* **6** 33–42
[72] Cukrov L M, Tsuzuki T and McCormick P G 2001 *Scr. Mater.* **44** 1787–90
[73] Indris S, Bork D and Heitjans P 2000 *J. Mater. Synth. Process.* **8** 245–50
[74] Kleinlogel C and Gauckler L J 2001 *Adv. Mater.* **13** 1081–5
[75] Chen I W and Wang X H 2000 *Nature* **404** 168–71
[76] Sánchez-López J C and Fernández A 2000 *Acta Mater.* **48** 3761–71
[77] Gissibl B, Wilhelm D, Würschum R, Herrig H, Müller F, Kelsch M, Reimann K, Phillipp F, Beck H P, Hempelmann R and Schaefer H-E 1997 *Nanostruct. Mater.* **9** 619–22
[78] Grom G F, Lockwood D J, McCaffrey J P, Labbé H J, Fauchet P M, White B Jr, Diener J, Kovalev D, Koch F and Tsybeskov L 2000 *Nature* **407** 358–61
[79] Puin W, Heitjans P, Dickenscheid W and Gleiter H 1993 *Defects in Insulating Materials* ed O Kanert and J Spaeth (Singapore: World Scientific) pp 137–9
[80] Puin W, Rodewald S, Ramlau R, Heitjans P and Maier J 2000 *Solid State Ion.* **131** 159–64
[81] Klug H P and Alexander L E 1959 *X-Ray Diffraction Procedures* (New York: Wiley)
[82] Krill C E, Haberkorn R and Birringer R 2000 *Handbook of Nanostructured Materials and Nanotechnology* vol 2, ed H S Nalwa (San Diego, CA: Academic) pp 165–97
[83] Krill C E and Birringer R 1998 *Phil. Mag.* A **77** 621–40
[84] Warren B E 1969 *X-Ray Diffraction* (London: Addison-Wesley)
[85] Warren B E and Averbach B L 1952 *J. Appl. Phys.* **23** 497
[86] Indris S and Heitjans P 2000 *Mater. Sci. Forum* **343–346** 417–22
[87] Heitjans P and Indris S 2002 *Synthesis, Functional Properties and Applications of Nanostructures (MRS 2001 Spring Proc. vol 676)* ed H W Hahn, D L Feldheim, C P Kubiak, R Tannenbaum and R W Siegel (Pittsburgh, PA: Materials Research Society) p Y6.6.1
[88] Indris S, Heitjans P, Haeger A and Hesse D 2003 to be published
[89] Eckert J, Holzer J C, Krill C E III and Johnson W L 1992 *J. Mater. Res.* **7** 1980–3
[90] Rüscher C H, Tobschall E and Heitjans P 2000 *Applied Mineralogy* ed D Rammlmair, J Mederer, Th Oberthür, R B Heiman and H Pentinghaus (Rotterdam: A A Balkema) pp 221–4
[91] Weirich Th E, Winterer M, Seifried S, Hahn H and Fuess F 2000 *Ultramicroscopy* **81** 263–70
[92] Würschum R, Soyez G and Schaefer H-E 1993 *Nanostruct. Mater.* **3** 225–30

[93] Brook H C, Chadwick A V, Kennedy K M, Morgante N, Rafeletos G, Tomba A and Roberts M A 1997 *Mater. Sci. Forum* **239–241** 683–6
[94] Rush G E, Chadwick A V, Kosacki I and Anderson H U 2000 *J. Phys. Chem.* B **104** 9597–606
[95] Mehrer H and Wenwer F 1998 *Diffusion in Condensed Matter* ed J Kärger, P Heitjans and R Haberlandt (Berlin: Springer) pp 1–39
[96] Crank J 1975 *The Mathematics of Diffusion* (Oxford: Clarendon)
[97] Einstein A 1905 *Ann. Phys., Lpz.* **17** 549–60
[98] von Smoluchowski M 1906 *Ann. Phys., Lpz.* **21** 756–780
[99] Funke K 1993 *Prog. Solid State Chem.* **22** 111–95
[100] Rickert H 1982 *Electrochemistry of Solids—An Introduction* (Berlin: Springer)
[101] Heitjans P and Schirmer A 1998 *Diffusion in Condensed Matter* ed J Kärger, P Heitjans and R Haberlandt (Berlin: Springer) pp 116–43
[102] Franke W and Heitjans P 1992 *Ber. Bunsenges. Phys. Chem.* **96** 1674–7
[103] Winter R, Siegmund K and Heitjans P 1997 *J. Non-Cryst. Solids* **212** 215–24
[104] Küchler W, Heitjans P, Payer A and Schöllhorn R 1994 *Solid State Ion.* **70/71** 434–8
[105] Bénière F 1972 *Physics of Electrolytes* ed J Hladik (London: Academic) pp 203–98
[106] Murch G E 1982 *Solid State Ion.* **7** 177–98
[107] Kubo R, Toda M and Hashitsume N 1991 *Statistical Physics II—Nonequilibrium Statistical Mechanics* (Berlin: Springer)
[108] Bunde A, Maass P and Meyer M 1998 *Diffusion in Condensed Matter* ed J Kärger, P Heitjans and R Haberlandt (Berlin: Springer) pp 319–39
[109] Heitjans P 1986 *Solid State Ion.* **18/19** 50–64
[110] Kärger J, Heitjans P and Haberlandt R (ed) 1998 *Diffusion in Condensed Matter* (Berlin: Springer)
[111] Le Claire A D 1970 *Physical Chemistry–An Advanced Treatise* vol 10, ed H Eyring, D Henderson and W Jost (New York: Academic) pp 261–330
[112] Compaan K and Haven Y 1958 *Scr. Mater.* **54** 1498–508
[113] Le Claire A D 1976 *Treatise on Solid State Chemistry* vol 4, ed N B Hannay (New York: Plenum) pp 1–59
[114] Bée M 1988 *Quasielastic Neutron Scattering* (Bristol: Adam Hilger)
[115] Schatz G and Weidinger A 1992 *Nuclear Condensed Matter Physics* (New York: Wiley)
[116] Heisel B, Hempelmann R, Hartmann O and Wäppling R 2000 *Physica* B **289/290** 487–90
[117] Checchetto R, Miotello A and Brusa R S 2001 *J. Phys.: Condens. Matter* **13** 5853–64
[118] McDonald J R (ed) 1983 *Impedance Spectroscopy* (New York: Wiley)
[119] Chadwick A V 1991 *Phil. Mag.* A **64** 983–98
[120] Badwal S P S and Rajendran S 1994 *Solid State Ion.* **70/71** 83–95
[121] Fleig J 2000 *Solid State Ion.* **131** 117–27
[122] Bauerle J E 1969 *J. Phys. Chem.* **30** 2657–70
[123] Gerhardt R and Nowick A S 1986 *J. Am. Ceram. Soc.* **69** 641–6
[124] Gerhardt R, Nowick A S, Mochel M E and Dumler I 1986 *J. Am. Ceram. Soc.* **69** 647–51
[125] Gödickemeyer M, Michel B, Orliukas A, Bohac P, Sasaki K, Gauckler L, Heinrich H, Schander P, Kostorz G, Hoffmann H and Frei O 1994 *J. Mater. Res.* **9** 1228–40
[126] Ioffe A I, Inozemtsev M V, Lipilin A S, Perfilev M V and Karpachov S V 1975 *Phys. Status Solidi* a **30** 87–95
[127] Chu S H and Seitz M A 1987 *J. Solid State Chem.* **23** 297–314
[128] Verkerk M J, Middelhuis B J and Burggraaf A J 1982 *Solid State Ion.* **6** 159–70
[129] Aoki M, Chiang Y-M, Kosacki I, Lee L J-R, Tuller H and Liu Y 1996 *J. Am. Ceram. Soc.* **79** 1169–80
[130] Wilkening M, Bork D, Indris S and Heitjans P 2002 *Phys. Chem. Chem. Phys.* **4** 3246–51
[131] Fukushima E and Roeder S B W 1981 *Experimental Pulse NMR* (Reading, MA: Addison-Wesley)
[132] Bloembergen N, Purcell E M and Pound R V 1984 *Phys. Rev.* **73** 679–712
[133] Abragam A 1999 *The Principles of Nuclear Magnetism* (Oxford: Oxford University Press)
[134] Slichter C P 1996 *Principles of Magnetic Resonance* (Berlin: Springer)
[135] Heitjans P, Körblein A, Ackermann H, Dubbers D, Fujara F and Stöckmann H-J 1985 *J. Phys. F: Met. Phys.* **15** 41–54
[136] Bork D and Heitjans P 2001 *J. Phys. Chem.* B **105** 9162–70
[137] Winter R and Heitjans P 2001 *J. Phys. Chem.* B **105** 6108–15
[138] Tobschall E 1999 *Dissertation* Universität Hannover
[139] Indris S, Heitjans P, Roman H E and Bunde A 2000 *Phys. Rev. Lett.* **84** 2889–92
[140] Indris S and Heitjans P 2002 *J. Non-Cryst. Solids* **307–310** 555–64
[141] Wilkening M, Indris S and Heitjans P 2003 *Phys. Chem. Chem. Phys.* **5** 2225–31
[142] Mondal P, Klein A, Jaegermann W and Hahn H 1999 *Solid State Ion.* **118** 331–9

[143] Lee J, Hwang J H, Mashek J J, Mason F O, Miller A E and Siegel R W 1995 *J. Mater. Res.* **10** 2295–300
[144] Chiang Y-M, Lavik E B, Kosacki I, Tuller H L and Ying J Y 1997 *J. Electroceram.* **1** 7–14
[145] Li G, Li L, Feng S, Wang M, Zhang L and Yao X 1999 *Adv. Mater.* **11** 146–9
[146] Kosacki I and Anderson H U 1996 *Appl. Phys. Lett.* **69** 4171–3
[147] Brossmann U, Würschum R, Södervall U and Schaefer H-E 1999 *Nanostruct. Mater.* **12** 871–4
[148] Knauth P and Tuller H L 1999 *J. Appl. Phys.* **85** 897–902
[149] Brossmann U, Södervall U, Würschum R and Schaefer H-E 1999 *J. Appl. Phys.* **85** 7646–54
[150] Schäfer H E 1993 *Defects in Insulating Materials* vol 33, ed O Kanert and J M Spaeth (Singapore: World Scientific) pp 122–36
[151] Divinski S V, Hisker F, Kang Y-S, Lee J-S and Herzig C 2002 *Z. Metallk.* **93** 256–64
[152] Knauth P 2002 *J. Solid State Electrochem.* **147** 115–21
[153] Knauth P and Tuller H L 2000 *Solid State Ion.* **136–137** 1215–24
[154] Tuller H L 2000 *Solid State Ion.* **131** 143–57
[155] Chiang Y-M, Lavik E B, Kosacki I, Tuller H L and Ying J Y 1996 *Appl. Phys. Lett.* **69** 185–7
[156] Tschöpe A, Sommer E and Birringer R 2001 *Solid State Ion.* **139** 255–65
[157] Tschöpe A 2001 *Solid State Ion.* **139** 267–80
[158] Nan C-W, Tschöpe A, Holten S, Kliem H and Birringer R 1999 *J. Appl. Phys.* **85** 7735–40
[159] Tarascon J-M and Armand M 2001 *Nature* **414** 359–67
[160] Poizot P, Laruelle S, Gruegeon S, Dupont L and Tarascon J-M 2000 *Nature* **407** 496–9
[161] Beaulieu L Y, Larcher D, Dunlap R A and Dahn J R 2000 *J. Electrochem. Soc.* **147** 3206–12
[162] Puin W and Heitjans P 1995 *Nanostruct. Mater.* **6** 885–8
[163] Leonhardt M, Jamnik J and Maier J 1999 *Electrochem. Solid-State Lett.* **2** 333–5
[164] Weppner W and Huggins R A 1978 *Annu. Rev. Mater. Sci.* **8** 269–311
[165] Kvist A 1972 *Physics of Electrolytes* ed J Hladik (London: Academic) pp 319–46
[166] Liang C C 1973 *J. Electrochem. Soc.* **120** 1289–92
[167] Maier J 1984 *Ber. Bunsenges. Phys. Chem.* **88** 1057–62
[168] Dudney N J 1989 *Annu. Rev. Mater. Sci.* **19** 113–20
[169] Filal M, Petot C, Mokchah M, Chateau C and Carpentier J L 1995 *Solid State Ion.* **80** 27–35
[170] Bunde A, Dieterich W and Roman H E 1985 *Phys. Rev. Lett.* **55** 5–8
[171] Roman H E, Bunde A and Dieterich W 1986 *Phys. Rev.* B **34** 3439–45
[172] Roman H E 1990 *J. Phys.: Condens. Matter* **2** 3909–17
[173] Debierre J-M, Knauth P and Albinet G 1997 *Appl. Phys. Lett.* **71** 1335–7
[174] Knauth P, Albinet G and Debierre J-M 1998 *Ber. Bunsenges. Phys. Chem.* **102** 945–52
[175] Knauth P 2000 *J. Electroceram.* **5** 111–25
[176] Sata N, Ebermann K, Eberl K and Maier J 2000 *Nature* **408** 946–9
[177] Indris S, Heitjans P, Roman H E and Bunde A 2001 *Defect Diffus. Forum* **194–199** 935–40
[178] Bork D and Heitjans P 1996 *28th Congr. Ampere on Magnetic Resonance and Related Phenomena* ed M E Smith and J H Strange (Canterbury: University of Kent) pp 418–19
[179] Winter R and Heitjans P 1999 *Nanostruct. Mater.* **12** 883–6
[180] Winter R and Heitjans P 2001 *J. Non-Cryst. Solids* **293–295** 19–24
[181] Bork D and Heitjans P 1998 *J. Phys. Chem.* B **102** 7303–6
[182] Rhim W-K, Burum D P and Ellemann D D 1978 *J. Chem. Phys.* **68** 692–5
[183] Meyer M, Maass P and Bunde A 1993 *Phys. Rev. Lett.* **71** 573–5
[184] personal communication Bork D, Fischer D M, Heitjans P, Winter R, Greaves N and Dent A 2002
[185] Whittingham M S 1978 *Prog. Solid State Chem.* **12** 41–99